


# Superconductivity near a Ferroelectric Quantum Critical Point in Ultralow-Density Dirac Materials

Vladyslav Kozii,<sup>1,\*</sup> Zhen Bi,<sup>1,\*</sup> and Jonathan Ruhman<sup>2,\*</sup>

<sup>1</sup>*Department of Physics, Massachusetts Institute of Technology, Cambridge, Massachusetts 02139, USA*

<sup>2</sup>*Department of Physics, Bar Ilan University, Ramat Gan 5290002, Israel*

 (Received 14 February 2019; revised manuscript received 28 May 2019; published 12 September 2019)

The experimental observation of superconductivity in doped semimetals and semiconductors, where the Fermi energy is comparable to or smaller than the characteristic phonon frequencies, is not captured by the conventional theory. In this paper, we propose a mechanism for superconductivity in ultralow-density three-dimensional Dirac materials based on the proximity to a ferroelectric quantum critical point. We derive a low-energy theory that takes into account both the strong Coulomb interaction and the direct coupling between the electrons and the soft phonon modes. We show that the Coulomb repulsion is strongly screened by the lattice polarization near the critical point even in the case of a vanishing carrier density. Using a renormalization group analysis, we demonstrate that the effective electron-electron interaction is dominantly mediated by the transverse phonon mode. We find that the system generically flows towards strong electron-phonon coupling. Hence, we propose a new mechanism to simultaneously produce an attractive interaction and suppress strong Coulomb repulsion, which does not require retardation. For comparison, we perform the same analysis for covalent crystals, where lattice polarization is negligible. We obtain qualitatively similar results, though the screening of the Coulomb repulsion is much weaker. We then apply our results to study superconductivity in the low-density limit. We find a strong enhancement of the transition temperature upon approaching the quantum critical point. Finally, we also discuss scenarios to realize a topological  $p$ -wave superconducting state in covalent crystals close to the critical point.

DOI: [10.1103/PhysRevX.9.031046](https://doi.org/10.1103/PhysRevX.9.031046)

Subject Areas: Superconductivity

## I. INTRODUCTION

A key step in the formation of a superconductor is the pairing between electrons. In spite of the strong Coulomb repulsion in free space, at a low energy, electrons experience an effective attraction in the presence of a lattice. Thus, superconductivity essentially relies on a mechanism that simultaneously reduces the Coulomb repulsion and generates a strong attractive interaction.

In simple (elemental) metals, such an attraction originates from the interchange of longitudinal phonons, which couple to the electronic density. To allow for this attraction to overcome the Coulomb repulsion, however, it is essential that the crystal vibrations are much slower than electronic motion. In terms of energy scales, this requirement implies that the Fermi energy is much larger than the Debye frequency. In the intermediate frequency regime, between

these two scales, the Coulomb repulsion is logarithmically suppressed, while the phonon interaction is unaffected [1–3]. As a result, the net interaction between electrons may become attractive below the Debye energy.

From this perspective, systems of low carrier concentration, such as doped semimetals and semiconductors, are not expected to exhibit superconductivity. First, they have a low Fermi energy, which is comparable to, or even smaller than, the typical Debye frequency and, thus, does not allow for the dynamical screening of the repulsion. Moreover, the superconducting transition temperature is exponentially sensitive to the density of states, which is typically 2 orders of magnitude smaller in doped semimetals and semiconductors compared to standard metals. Thus, naively, attainable transition temperatures require an unphysically large interaction strength.

Surprisingly, however, superconductivity in doped semimetals and semiconductors is ubiquitous. It was first discovered in SrTiO<sub>3</sub> [4] and later in many other materials [5]. To the best of our knowledge [6], the lowest-density superconductors discovered to date are Tl-doped PbTe [8], Sr-doped Bi<sub>2</sub>Se<sub>3</sub> [9], YPtBi [10], SrTiO<sub>3-x</sub> [11,12], and elemental bismuth [13]. It is noteworthy that, except for SrTiO<sub>3</sub>, all of these materials are either narrow-band

\*All authors contributed equally.

*Published by the American Physical Society under the terms of the Creative Commons Attribution 4.0 International license. Further distribution of this work must maintain attribution to the author(s) and the published article's title, journal citation, and DOI.*

topological insulators or topological semimetals. The common feature they share is a near crossing of their conduction and valence bands, for example, such as in Dirac material. These experiments, thus, impose two theoretical challenges: (i) How is the Coulomb repulsion screened when the dynamical timescale of the pairing interaction is comparable to, or even smaller than, the electronic timescale (the so-called antiadiabatic limit)? (ii) What is the source of attraction, which is strong enough to deal with such a small density of states?

A variety of theoretical frameworks have been proposed to discuss superconductivity in the limit of low density, including polar phonons [14–18], plasmons [15,19–21], multiband effects [22,23], soft optical phonons [24], negative  $U$  centers [25], and instantaneous attraction [26,27]. It is particularly important to single out the seminal contribution of the authors of Ref. [14], who point out an essential ingredient in any theory of low-density superconductivity: a long-ranged attractive interaction. When the range of the attractive interaction is comparable to the distance between conduction electrons, it naturally competes with the small density of states and, thus, paves the way to solve the second theoretical challenge we specify above. This situation is similar to the phenomenon of Wigner crystallization, where the long-ranged Coulomb interaction dominates the kinetic energy in the dilute limit rather than at a high density. Thus, the constraint of long-ranged attraction narrows down the range of viable pairing mechanisms in the extreme low-density limit. Such an interaction may result from a dynamically screened Coulomb repulsion [14,19], fluctuations of an order parameter close to a quantum critical point [28–31], spin fluctuations [32,33], or Goldstone mode fluctuations in certain types of spontaneously broken continuous symmetries [34].

It is interesting to notice that SrTiO<sub>3</sub>, PbTe, and SnTe naturally reside close to a paraelectric (PE)-ferroelectric (FE) phase transition [35,36], which can be tuned in various manners. Indeed, it has been proposed theoretically that the superconducting state in low-density SrTiO<sub>3-x</sub> results from a pairing interaction mediated by FE fluctuations near the quantum critical point (QCP) [37]. Following this proposal, recent experiments report an enhancement of  $T_c$  in the vicinity of the QCP [17,38–40]. This proposal also leads to a number of theoretical studies discussing different aspects of the problem [41–44]. However, an important question that remains open is the microscopic origin of a strong electronic coupling to the soft FE fluctuations, which is naïvely expected to be weak [45–47] (we also refer to a recent comment on the subject [48] and the recent preprint [49]).

To explain the origin of the common belief concerning weak coupling between electrons and soft FE modes in low-density ionic crystals, we briefly review some basic facts regarding the FE QCP. The PE-FE transition is essentially a structural transition where the order parameter

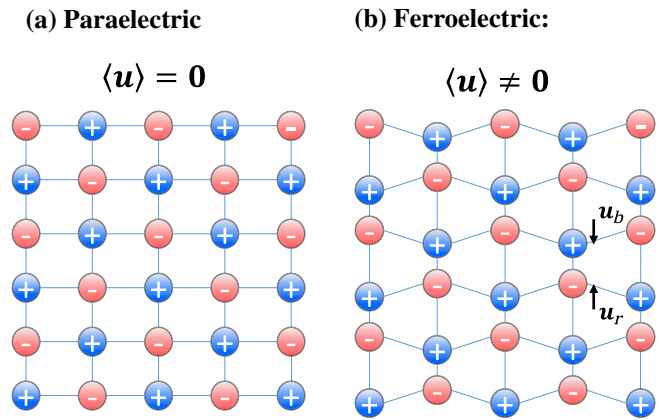


FIG. 1. (a) A diatomic cubic ionic crystal in the paraelectric phase. The two ions are represented by blue (+) and red (–) circles (e.g., blue for Pb and red for Te). Unless these two atoms are identical, they will have an average charge imbalance. (b) The ferroelectric phase (inversion breaking) is characterized by a uniform optical phonon displacement vector  $\mathbf{u} = \mathbf{u}_b - \mathbf{u}_r$ . Because of the charge imbalance between the ions, this phase is also characterized by a finite dipolar polarization density  $\mathbf{P} = Q\mathbf{u}$ , where  $Q$  is the charge.

is a vector (i.e., a lattice distortion), which spontaneously breaks inversion and rotation symmetries in the ordered state. As an example, we consider the diatomic ionic crystal in Fig. 1. In the FE phase, the two ions in the unit cell are distorted from their cubic Bravais lattice positions. Because of a charge imbalance, the ions induce a uniform electric polarization density. Thus, the transition is described by a soft optical phonon mode associated with the relative displacement of the two charged ions. This phonon mode has three polarizations: one longitudinal optical (LO) and two transverse optical (TO). The long-range dipolar interactions between lattice distortions, however, prevent the LO mode from softening near the transition [35,50–53]. Consequently, the soft bosonic modes associated with the FE QCP are purely transverse. On the other hand, the simplest coupling between the conduction electrons' density and lattice is Fröhlich coupling, which involves only longitudinal modes [45,47,54]. As a result, the interaction between electrons and soft FE modes is typically considered as weak.

Despite the above discussion, the direct coupling of gapless electrons to soft transverse phonon (ferroelectric) modes is possible in multiorbital systems [55,56]. For time-reversal symmetric systems with a single Fermi surface, multiorbital effects can manifest themselves only due to the presence of spin-orbit coupling [57,58]. In this paper, we use this idea to explicitly derive a complete low-energy theory capturing all gapless degrees of freedom at the FE QCP in three-dimensional Dirac materials, a manifestly multiorbital system with strong spin-orbit coupling, and show how transverse modes couple to gapless electrons in the long-wavelength limit. We use the renormalization

group (RG) approach to study the tendency of this theory towards strong coupling close to the critical point. We find that the proximity to the FE QCP in the low-density limit leads to strong screening of the Coulomb repulsion between electrons by the crystal. Concomitantly, the interband transitions across the Dirac point enhance the effective coupling of electrons to the soft TO phonon modes.

Thus, the attraction mediated by TO modes generically overcomes the Coulomb repulsion close to a FE QCP. Interestingly, this result is valid even at a vanishing electronic density, when the effects of Coulomb repulsion are expected to be strong. Therefore, our theory is distinct from the standard Tolmachev-Anderson-Morel mechanism [1–3], since it does not require the phonon frequency to be smaller than the Fermi energy in order to produce net attraction at zero frequency. Finally, we analyze the possible superconducting instabilities from the interaction mediated by the critical phonon mode. We find a strong enhancement of the transition temperature  $T_c$  due to the enhancement of the electron-phonon coupling close to the critical point.

For completeness and comparison, we perform a similar analysis for covalent (nonionic) crystals, where both LO and TO modes are soft at the critical point. In this case, negligible lattice polarization does not allow for a spontaneous dipolar moment of the crystal, so a “ferroelectric” phase is simply characterized by broken inversion symmetry. In the absence of lattice polarization the screening of the Coulomb interaction is only logarithmic, similar to the case without soft phonons [59,60]. We find that the dimensionless coupling constant associated with the coupling to the longitudinal mode also flows logarithmically to zero, while the coupling to transverse modes remains relevant, as before. Thus, our result is an example where attraction may overcome repulsion without any requirement on the Fermi energy, even without screening from the crystal. We point out that this result is potentially relevant to other nonpolar critical modes that couple to Dirac points. We also find that the interplay between phonon-mediated attraction and the Coulomb repulsion in these covalent crystals opens a possibility of topological  $p$ -wave superconductivity in a certain range of parameters.

Beside the fundamental theoretical importance, our study of superconductivity from ferroelectric quantum critical fluctuations is also motivated by a realistic system: the ionic alloy  $\text{Pb}_{1-z}\text{Sn}_z\text{Te}$ , which undergoes a FE phase transition at  $z = z_{\text{FE}} \approx 0.25$  [36]. When  $z$  is further increased above  $z_T \approx 0.41$ , the alloy undergoes a second, topological phase transition, between a trivial insulator and a topological crystalline insulator [61]. The topological transition entails gapless Weyl points close to the  $L$  points of the Brillouin zone [62]. When doped with Tl or In atoms, this alloy becomes superconducting, and the transition temperature exhibits a peak at some intermediate value of  $z$  [63]. While doped  $\text{Pb}_{1-z}\text{Sn}_z\text{Te}$  seems a promising

candidate for our theory, a word of caution is needed, since certain features require further understanding. In pure PbTe, for example, superconductivity appears only when doped with Tl. Additionally, it is found that the superconducting state emerges only above a critical density, where additional electron pockets become populated [64].

The remainder of the paper is organized as follows. We first summarize our main results while providing intuitive pictures in Sec. II. In Sec. III, we present a complete low-energy theory for Dirac materials near a FE QCP. In Sec. IV, we use the RG approach to demonstrate that the Coulomb repulsion is strongly screened by lattice polarization, while the coupling between electrons and soft transverse phonons is significantly enhanced. We find qualitatively similar results for covalent crystals, though the screening of Coulomb repulsion in this case is much weaker because of negligible lattice polarization. Finally, in Sec. V, we analyze the possible superconducting instabilities from the interaction mediated by the critical phonon (ferroelectric) mode. We find a strong enhancement of the transition temperature  $T_c$  due to the enhancement of the electron-phonon coupling close to the critical point. Additionally, we discuss scenarios for  $p$ -wave superconductivity originating from the interplay between phonon-mediated attraction and Coulomb repulsion in covalent crystals. We finish with a short summary and discussion in Sec. VI.

## II. SUMMARY OF MAIN RESULTS

Before moving on to the main part of the paper, where we carefully analyze the FE QCP in a Dirac system using the RG technique, we first present our main results at a nontechnical level. We aim to qualitatively explain how our findings deal with the long-standing challenge of understanding superconductivity in low-density systems.

As explained in the introduction, the observation of superconductivity in extremely dilute metals poses two questions which are the main focus of this paper.

- (i) How is the Coulomb repulsion screened in a system with a relatively small Fermi energy (the so-called antiadiabatic limit)?
- (ii) What is the source for strong attraction that can overcome the small density of states in these systems?

To answer these questions, we focus on a concrete model consisting of three essential ingredients, which are all mutually coupled (see Fig. 2). The ingredients are fluctuations of the FE order parameter close to a FE QCP (optical phonon distortions), gapless Dirac fermions, and the static electric field [65].

The key new element that plays a crucial role in our study is the direct coupling  $\lambda$  between electrons and optical phonons (especially the TO modes). The coupling is allowed in materials with strong spin-orbit coupling such as Dirac semimetals. The intuitive picture behind this coupling is the following: When the unit cell distorts

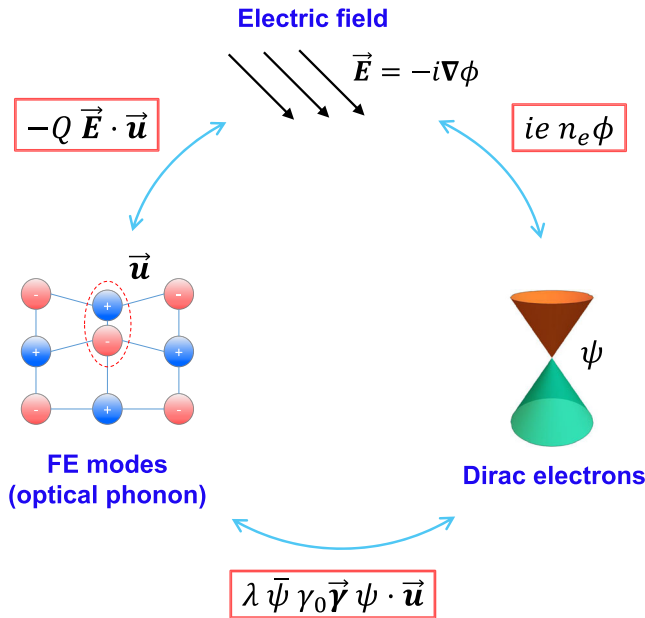


FIG. 2. The three fields participating in the low-energy effective field theory Eq. (8) and the couplings between them. The fields are the ferroelectric fluctuations (optical phonon distortions), Dirac electrons, and *static* electric field. The coupling of the ferroelectric mode to the electric field leads to the gapping out of the longitudinal optical mode (LO-TO splitting) and to the well-known Fröhlich coupling; see Eq. (12). The coupling of the electrons to the electric field generates the Coulomb repulsion. An important new element, which is one of the key points of the paper, is the direct coupling  $\lambda$  between the optical phonon distortions and the Dirac electrons; see Eq. (7).

due to a FE optical phonon, inversion symmetry is locally broken. In the presence of spin-orbit coupling, this distortion induces a Rashba effect modifying the electronic dispersion, thus coupling electrons to phonons.

Interestingly, the first question raised above, screening of the Coulomb repulsion in the antiadiabatic limit, is naturally dealt with in this model. In the case of ionic crystals, the polar phonons provide the screening. The important prerequisite, however, is the proximity of the system to a FE QCP. Indeed, according to the Lyddane-Sachs-Teller relation [66], the low-energy dielectric constant behaves as  $\epsilon_0 \sim \omega_L^2/\omega_T^2$  [66]. At the FE QCP, the TO phonon frequency vanishes, while the LO phonon remains gapped due to its polar nature (see the inset in Fig. 3 for a schematic dispersion). Consequently,  $\omega_T \rightarrow 0$ , while  $\omega_L$  remains finite near the FE QCP, so  $\epsilon_0$  diverges, leading to the suppression of the long-ranged Coulomb interaction. Additionally, we find that, even in the absence of crystal screening (like in covalent crystals that we discuss below), the interband transitions across the Dirac dispersion also effectively screen the Coulomb repulsion in the antiadiabatic limit.

To deal with the second question about the source of the sufficiently strong attraction between electrons, we recall the seminal result by Gurevich, Larkin, and Firsov [14],

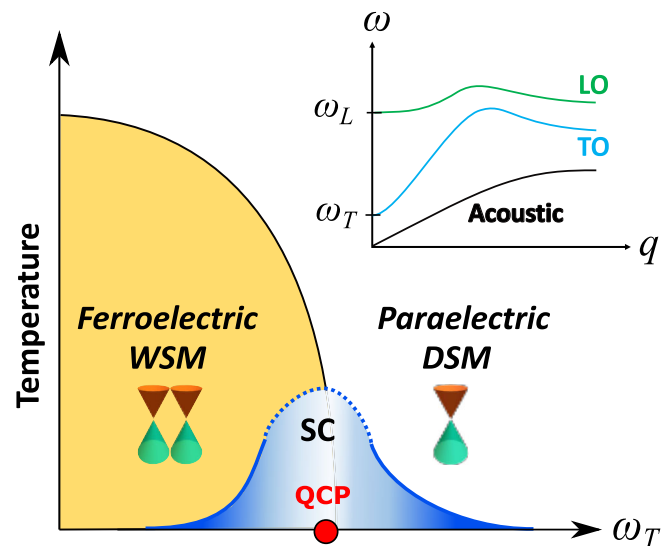


FIG. 3. Schematic phase diagram of the 3D Dirac semimetal (DSM) near a FE QCP. The FE QCP separates the inversion-symmetric DSM and inversion-broken Weyl semimetal (WSM) phases. Upon approaching the phase transition (controlled by  $\omega_T$ ), there is a region where we predict superconductivity at an ultralow density (blue dome). Because of the long-ranged dipolar forces between LO modes, close to the FE QCP, only the TO modes soften, as shown in the inset (the LO-TO splitting). We consider the direct coupling of these TO modes to the Dirac fermions through spin-orbital effects. RG analysis shows that this coupling is a relevant perturbation that renders the Dirac point unstable at a low energy. We find that this type of QCP combines two ingredients which are essential for superconductivity at a low density: (i) strong attraction that compensates a small density of states and (ii) screening of the Coulomb repulsion between electrons by the LO modes. The dashed line denotes the region of strong coupling in the immediate vicinity of the critical point where our weak-coupling analysis breaks down.

who point out that the low-density SC necessarily requires a long-ranged interaction. In our theory, there are two key elements that provide such an interaction. First, near the FE QCP, we have a soft (nearly gapless) TO phonon mode. This fact itself, however, does not guarantee the long-ranged interaction; otherwise, the acoustic phonons would be sufficient for this purpose. The crucial element of our theory that allows for such a long-ranged interaction is exactly the direct coupling between electrons and optical phonons  $\lambda$  that we discuss above. Indeed, this coupling does not vanish at a small momentum transfer and is generically present in 3D Dirac materials. Then, it is straightforward to show that the effective attraction between electrons mediated by TO phonons is sufficiently long ranged, which compensates the low density of states. Putting all the described key points together, we conclude that the combination of a finite electron-phonon coupling and the proximity to the FE QCP is sufficient for superconductivity in the low-density 3D Dirac materials. This result is schematically summarized in Fig. 3.

To make the above arguments more quantitative and rigorous, we study our model using the renormalization group technique. In particular, we find that, in the weak-coupling regime, the dimensionless coupling constant between electrons and TO phonons,  $\beta$ , is marginally relevant [see Eqs. (17) and (27)] and, hence, gets enhanced at small energies. The main origin of this enhancement is the reduction of the TO phonon velocity due to a cloud of virtual particle-hole excitations that is generated as it propagates through the crystal. The velocity reduction increases the TO phonon density of states at low energies, which enhances the resulting phonon-mediated interaction. The particle-hole excitations, which are responsible for the velocity reduction, are of the interband type (i.e., across the Dirac node). Therefore, the nearly touching between the conduction and valence bands, characterizing the Dirac dispersion, is important for the enhancement of  $\beta$ . This enhancement, in turn, leads to a sufficient increase in the superconducting transition temperature  $T_c$ ; see Eqs. (35) and (36).

As a final step, we calculate the superconducting instabilities with the renormalized parameters. We work within the weak-coupling approximation and assume a small but finite Fermi surface with the radius  $k_F$ . We find that the strongest superconducting instability is in the  $s$ -wave channel, but the vector-type  $p$  wave also exhibits weaker instability towards the Cooper pairing. For these two channels, we compute the corresponding transition temperatures; see Eqs. (35)–(37). As is usual for a weak-coupling approximation,  $T_c$  is exponentially sensitive to the renormalized dimensionless coupling  $\beta^*$  and the square of the ratio  $k_F/\Lambda_r$ , where  $\Lambda_r$  can be viewed as the inverse correlation length of the FE order parameter or, equivalently, the range of the TO phonon-mediated attraction between electrons. Since we find  $\beta$  to be a relevant operator, both  $\beta^*$  and  $k_F/\Lambda_r$  can be made of the order of 1 near the FE QCP, thus leading to a significantly large transition temperature despite the low density of states. Our rough estimates show that one can reach  $T_c$  of the order of several Kelvin sufficiently close to the critical point even at densities  $n_0 \sim 10^{17} \text{ cm}^{-3}$ .

The above discussion is relevant for ionic crystals. For completeness, we also consider the case of covalent crystals, where the atoms in Fig. 1 would be neutral, and, thus, the optical phonons would be decoupled from the electric field. In this case, the LO mode is also gapless at the transition point, and, consequently, it no longer screens the Coulomb interaction. Our RG analysis shows that the same interband processes that enhance the coupling  $\beta$  suppress the fine-structure constant  $\alpha$  and the coupling to the LO phonon  $\tilde{\beta}$ ; see Eqs. (24) and (25). The former is simply the interband screening of the Coulomb interaction [59]. Consequently, the end result is qualitatively the same: At the critical point, the TO phonon-mediated interaction is the dominant one, and there is still a mechanism to screen

the Coulomb repulsion, which does not rely on retardation (in this case, it is purely electronic). The crucial difference, however, is that the screening of the Coulomb interaction is only logarithmic and, consequently, weaker than in the case of ionic crystals. The fact that crystal screening is not necessary to suppress the Coulomb repulsion at scales higher than the Fermi level also implies that our analysis for the FE QCP can be extended to other types of critical points in Dirac semimetals. The fact that almost all known low-density superconductors carry semimetallic features in their band structure raises the question of whether such an antiadiabatic screening of the Coulomb repulsion plays an important role in the emergence of superconductivity in these systems.

### III. MODEL

We now turn to the main part of the paper. We first consider the low-energy effective field theory of a Dirac semimetal near the ferroelectric transition. The Euclidean (imaginary time) action is given by the sum

$$\mathcal{S} = \mathcal{S}_\psi + \mathcal{S}_u + \mathcal{S}_\phi + \mathcal{S}_{\psi u} + \mathcal{S}_{\psi\phi} + \mathcal{S}_{u\phi}, \quad (1)$$

where the first three terms describe the dynamics of the fermions  $\psi$ , the optical phonon field  $u$ , and the Coulomb field  $\phi$ , respectively, while the latter three describe their interactions. The Coulomb field  $\phi$  should be considered as a Hubbard-Stratonovich decomposition of the instantaneous Coulomb interaction. Now we specify these terms in detail.

#### A. Quadratic terms

##### 1. The electron term

The electron quadratic term (motivated by the model of the PbTe crystal [61]) reads

$$\mathcal{S}_\psi = \sum_{n=1}^N \int d^4x \bar{\psi}_n (\gamma_0 \partial_0 + v_F \gamma_j \partial_j + m - \gamma_0 \varepsilon_F) \psi_n, \quad (2)$$

where  $\psi_n$  is a four-component Dirac spinor,  $n = 1, \dots, N$  denotes different fermionic flavors (number of Dirac nodes), summation over  $j = x, y, z$  is implied ( $\partial_0$  stands for the derivative in imaginary time), and  $\bar{\psi}_n \equiv \psi_n^\dagger \gamma^0$ . Parameters  $v_F$ ,  $m$ , and  $\varepsilon_F$  stand for the electron velocity, Dirac mass, and Fermi energy, respectively. We use Hermitian gamma matrices  $\{\gamma_0, \gamma_1, \gamma_2, \gamma_3\} = \{\sigma^1 \otimes \sigma^0, \sigma^2 \otimes \sigma^1, \sigma^2 \otimes \sigma^2, \sigma^2 \otimes \sigma^3\}$  and  $\gamma_5 = \gamma_0 \gamma_1 \gamma_2 \gamma_3$ , where  $\sigma_i$  are usual Pauli matrices. Notice that here we assume an isotropic dispersion by taking the same velocity  $v_F$  in all directions. The anisotropic case does not modify the main qualitative results of this paper, and, therefore, we comment on it in the Appendix D. For generality, we assume a nonzero mass term  $m$  and a finite Fermi energy  $\varepsilon_F$ . However, we

neglect them in our RG analysis, assuming that they are much smaller than other relevant energy scales.

We note two important discrete symmetries of Eq. (2): inversion symmetry  $\mathcal{P}$  and time-reversal symmetry  $\mathcal{T}$ . The action of these symmetries in terms of Dirac matrices is given by  $\mathcal{P} = \gamma_0$  and  $\mathcal{T} = \gamma_1\gamma_3K$ , respectively, where  $K$  is the complex conjugation.

## 2. The phonon term

Next, we consider the dynamics of the phonon modes, which become soft at the FE phase transition. To have an intuitive picture in mind, we consider the scenario in which the FE order is dominantly generated by a lattice distortion. For simplicity, we consider a cubic ionic crystal with two atoms in the unit cell (the rocksalt structure of the IV-VI semiconductors; see Fig. 1). We label the two sublattices by  $b$  and  $r$ , corresponding to the “blue” and “red” ions, respectively which have equal in magnitude and *opposite* sign charges. Each sublattice has a corresponding phonon displacement field  $\mathbf{u}_r$  and  $\mathbf{u}_b$ . As usual, there are two modes: a gapless acoustic mode given by the sum  $\mathbf{u}_{ac} = (\mathbf{u}_r + \mathbf{u}_b)/2$  and a gapped optical branch given by the difference  $\mathbf{u} = \mathbf{u}_r - \mathbf{u}_b$ . Near the FE transition, the acoustic mode is irrelevant, while the optical branch becomes nearly gapless and is described by the effective action

$$\mathcal{S}_u = \int d^4x \frac{1}{2} u_j [(-\partial_0^2 + \omega_T^2)\delta_{jl} - c_T^2(\nabla^2\delta_{jl} - \partial_j\partial_l) - c_L^2\partial_j\partial_l] u_l + V(u_j u_j)^2. \quad (3)$$

Here,  $c_L$  and  $c_T$  are the longitudinal and transverse phonon velocities, respectively,  $\omega_T$  is the phonon mass, which is the tuning parameter to the transition, and  $V$  is the lowest-order symmetry allowed anharmonic correction to the phonon energy (where we neglect additional anisotropic terms allowed by the cubic symmetry [50–53]). Again, summation over  $j, l = x, y, z$  is implied.

## 3. The Coulomb term

The third quadratic term describes the Coulomb potential:

$$\mathcal{S}_\phi = \frac{\epsilon_\infty}{8\pi} \int d^4x (\nabla\phi)^2, \quad (4)$$

where  $\epsilon_\infty$  is the bare dielectric constant, which accounts for the contribution of core electrons. This contribution is due to the transitions between the high-energy atomic configurations and does not include the contributions from the lattice dynamics or electronic interband transitions close to the Dirac point.

## B. Coupling terms

We now consider the couplings between the fields introduced in Eqs. (2)–(4).

### 1. Electron-Coulomb coupling

We start with the coupling between the Dirac electrons and the Coulomb potential

$$\mathcal{S}_{\psi\phi} = ie \int d^4x \rho_e \phi, \quad (5)$$

where  $\rho_e = \sum_n \bar{\psi}_n \gamma_0 \psi_n$  is the electronic density.

### 2. Phonon-Coulomb coupling

The coupling of the ferroelectric phonon modes to the Coulomb potential follows from Eq. (5) by noting that the deviations of the red and blue ionic density from the average equilibrium value  $\rho_0$  in the long-wavelength limit are given by  $\rho_r = \rho_0(1 - \nabla\mathbf{u}_r)$  and  $\rho_b = \rho_0(1 - \nabla\mathbf{u}_b)$ , respectively. Given that the ionic charges are of equal magnitude and opposite signs, the coupling of the lattice to the Coulomb field  $\phi$  is given by

$$\mathcal{S}_{u\phi} = iQ \int d^4x (\rho_r - \rho_b)\phi = iQ\rho_0 \int d^4x \nabla\mathbf{u}\phi, \quad (6)$$

where  $Q$  is the ionic charge on blue sites (the charge on red sites equals  $-Q$ ). For the purpose of further analysis, it is convenient to absorb factor  $\rho_0$  by redefining  $Q\rho_0 \rightarrow Q$ .

Notice that the form of the coupling (6) implies that only the *longitudinal* phonon mode couples to the Coulomb field. We also point out that, after integrating Eq. (6) by parts, one gets a dot product between the polarization density  $\mathbf{P} = Q\mathbf{u}$  and the electric field  $\mathbf{E} = -i\nabla\phi$ . Therefore, this equation can also be viewed as the action of a dipole moment density in an electric field. Finally, in the case of a nonpolar covalent crystal (e.g., elemental bismuth), all atoms in the unit cell are neutral, leading to a vanishing coupling  $Q = 0$ .

### 3. Electron-phonon coupling

We now consider the coupling between the Dirac electrons and the phonon modes. We write down this coupling from general symmetry arguments. The phonon mode  $\mathbf{u}$  is a time-reversal invariant vector. Inspecting all possible *local* Dirac bilinears specified in Table I, we find that the only Dirac bilinear that forms a time-reversal symmetric vector and, thus, is allowed to couple to the phonon displacement field is  $\bar{\psi}\gamma_0\gamma_j\psi$ . Therefore, the corresponding coupling is given by

$$\mathcal{S}_{\psi u} = \lambda \sum_{n=1}^N \int d^4x \bar{\psi}_n \gamma_0 \gamma_j \psi_n u_j. \quad (7)$$

The microscopic origin of this coupling is a combination of the interorbital hybridization induced by the lattice distortion  $\mathbf{u}$  and spin-orbit coupling. This situation is similar to the Rashba effect, which arises when inversion

TABLE I. Parity and time-reversal symmetry of the 16 ( $k$ -independent) Dirac bilinears.

Bilinear	$1, \gamma_0$	$\{i\gamma_1, i\gamma_2, i\gamma_3\}, i\gamma_5$	$\{\gamma_0\gamma_1, \gamma_0\gamma_2, \gamma_0\gamma_3\}, \gamma_0\gamma_5$	$\{i\gamma_0\gamma_1\gamma_5, i\gamma_0\gamma_2\gamma_5, i\gamma_0\gamma_3\gamma_5, i\gamma_0\gamma_1\gamma_2, i\gamma_0\gamma_1\gamma_3, i\gamma_0\gamma_2\gamma_3\}$
$\mathcal{P} = \gamma_0$	+	-	-	+
$\mathcal{T} = \gamma_0\gamma_2\gamma_5K$	+	-	+	-

is broken in a system with spin-orbit coupling. The analogy is made by noting that the optical phonon distortion is essentially an inversion-breaking field. It is also worth noting that the form of the coupling Eq. (7) can be derived from the action of inversion breaking on a Dirac node [67]. To estimate the magnitude of the coupling accurately, however, an *ab initio* calculation is required. Finally, we also note that in Eq. (2) we assume that the Dirac cones occur at the inversion symmetric points in the Brillouin zone. In the case where they do not, the coupling can also include interflavor scattering.

We emphasize that, for simplicity, we consider a rotationally symmetric model in the main text. We discuss the possible effects of the cubic anisotropy in Appendix D.

#### IV. RENORMALIZATION GROUP ANALYSIS NEAR THE CRITICAL POINT

We now use the RG to analyze the theory introduced in the previous section. Summing up Eqs. (2)–(7), we have

$$\mathcal{S} = \int d^4x \left\{ \sum_{n=1}^N \bar{\psi}_n [Z_\psi \gamma_0 \partial_0 + v_F \gamma_j \partial_j] \psi_n + \frac{1}{2} u_j [(-Z_u^2 \partial_0^2 + \omega_T^2) \delta_{jl} - c_T^2 (\nabla^2 \delta_{jl} - \partial_j \partial_l) - c_L^2 \partial_j \partial_l] u_l \right. \\ \left. + V(u_j^2)^2 + \frac{\varepsilon_\infty}{8\pi} (\partial_j \phi)^2 + ie \sum_{n=1}^N \bar{\psi}_n \gamma^0 \psi_n \phi + iQ\phi \partial_j u_j + \lambda \sum_{n=1}^N \bar{\psi}_n \gamma_0 \gamma_j \psi_n u_j \right\}. \quad (8)$$

The coefficients  $Z_\psi$  and  $Z_u$  account for the renormalization of the dynamical terms.

We apply the standard momentum-shell RG scheme [68] by separating fields into short- and long-scale parts according to  $\psi(\omega, \mathbf{q}) = \psi_>(\omega, \mathbf{q}) + \psi_<(\omega, \mathbf{q})$  (analogously with fields  $\mathbf{u}$  and  $\phi$ ), followed by the integrating out the high-energy part  $\psi_>(\omega, \mathbf{q})$  within an infinitesimal cylindrical momentum-frequency shell  $\Lambda_0 e^{-\delta l} < q < \Lambda_0$ ,  $-\infty < \omega < \infty$ . Here,  $\Lambda_0$  is a momentum UV cutoff corresponding to the scale at which electron dispersion can be considered linear, and  $l$  is ‘‘RG time.’’ As the second step, we further rescale momenta, frequencies, and the long-wavelength parts of the fields according to

$$\mathbf{q} = e^{-\delta l} \mathbf{q}', \quad \omega = e^{-z\delta l} \omega', \quad \psi_<(\omega, \mathbf{q}) = e^{\eta_\psi \delta l} \psi'(\omega', \mathbf{q}'), \\ \phi_<(\omega, \mathbf{q}) = e^{\eta_\phi \delta l} \phi'(\omega', \mathbf{q}'), \quad \mathbf{u}_<(\omega, \mathbf{q}) = e^{\eta_u \delta l} \mathbf{u}'(\omega', \mathbf{q}'), \quad (9)$$

to restore the UV cutoff  $e^{-\delta l} \Lambda_0$  back to  $\Lambda_0$ . Above,  $z$  is the dynamical exponent, and  $\eta_\psi$ ,  $\eta_u$ , and  $\eta_\phi$  are engineering field dimensions. This rescaling leads to the tree-level RG flows of the couplings after coarse-graining by the factor  $e^l$  (the argument  $l$  is suppressed for brevity):

$$Z_\psi/Z_\psi(0) = e^{(2\eta_\psi - 2z - 3)l}; \quad Z_u/Z_u(0) = e^{(\eta_u - 3z/2 - 3/2)l}, \\ c_{T,L}/c_{T,L}(0) = e^{(\eta_u - z/2 - 5/2)l}; \quad v_F/v_F(0) = e^{(2\eta_\psi - z - 4)l}, \\ \omega_T/\omega_T(0) = e^{(\eta_u - z/2 - 3/2)l}; \quad V/V(0) = e^{(4\eta_u - 3z - 9)l}, \\ e/e(0) = e^{(2\eta_\psi + \eta_\phi - 2z - 6)l}; \quad Q/Q(0) = e^{(\eta_u + \eta_\phi - z - 4)l}, \\ \lambda/\lambda(0) = e^{(2\eta_\psi + \eta_u - 2z - 6)l}; \quad \varepsilon_\infty/\varepsilon_\infty(0) = e^{(2\eta_\phi - 5 - z)l}. \quad (10)$$

It should be mentioned that the choice of dynamical and field exponents is somewhat arbitrary here, since it does not affect the flow of dimensionless coupling constants [69,70]. The special choice  $\omega_T^2 = 0$ ,  $Q = e = \lambda = 0$ ,  $\eta_\psi = 5/2$ ,  $\eta_u = \eta_\phi = 3$ , and  $z = 1$  makes the theory scale invariant, which corresponds to the noninteracting fixed point. Near this fixed point,  $\omega_T^2$  and  $Q$  are relevant perturbations, while  $e$  and  $\lambda$  are marginal at the tree level. Since  $\omega_T^2$  is the tuning parameter for the FE transition, we assume it to be small close to the critical point. In what follows, we focus on two distinct cases: the case of ionic crystals with  $Q \neq 0$  and the case of covalent crystals with  $Q = 0$ .

#### A. Ionic crystals ( $Q \neq 0$ )

##### 1. Fixed-point theory

Near the noninteracting fixed point introduced above,  $Q$  is relevant and, at the tree level, obeys the following RG equation:

$$\frac{dQ}{dl} = Q. \quad (11)$$

Thus, in the case of ionic crystals,  $Q$  grows rapidly to strong coupling. Therefore, we should first derive the effective low-energy theory with large coupling  $Q$  (of the order of the UV cutoff) and then proceed to the RG analysis of the resulting theory. We can integrate out the Coulomb field  $\phi$ , which generates the following terms:

$$\int D[\phi] e^{-S_\phi - S_{\psi\phi} - S_{u\phi}} \propto e^{-\int_{n,q} \mathcal{L}'};$$

$$\mathcal{L}' = \frac{2\pi}{\epsilon_\infty q^2} [e^2 |\delta\rho_e(q)|^2 + Q^2 |\mathbf{q} \cdot \mathbf{u}_q|^2 - 2eQiq \cdot \mathbf{u}_q \delta\rho_e(-q)]. \quad (12)$$

The first term is the standard Coulomb repulsion between electrons. The second term can be viewed as a phonon mass generated in the longitudinal sector (note that it is independent of the magnitude of the momentum). This mass generation is the well-known LO-TO splitting in ionic crystals [47]. Finally, the last term is the Fröhlich coupling between the longitudinal phonon mode and electronic density.

The generated mass term for the longitudinal phonon mode equals  $\omega_L \equiv \sqrt{4\pi Q^2/\epsilon_\infty + \omega_T^2}$ . While the transverse mode becomes massless near the FE transition,  $\omega_T \rightarrow 0$ , we see that the longitudinal mode remains massive, since  $Q \gg \omega_T$ . Consequently, the LO mode can be further integrated out. This procedure generates the standard dynamically screened Coulomb interaction between electrons:

$$S_C = \frac{1}{2} \int \frac{d\omega d^3q}{(2\pi)^4} \frac{4\pi e^2}{\epsilon(\omega, q) q^2} |\delta\rho_e|^2, \quad (13)$$

where

$$\epsilon(\omega, q) = \epsilon_\infty \frac{\omega^2 + \omega_L^2 + c_L^2 q^2}{\omega^2 + \omega_T^2 + c_L^2 q^2} \quad (14)$$

is the dynamical dielectric constant, which manifestly satisfies the Lyddane-Sachs-Teller relation [46,47,66].

Close to the critical point, we have  $\omega_T \rightarrow 0$ , which implies that the dielectric constant scales as  $\epsilon(\omega, q) \approx \epsilon_\infty \omega_L^2 / (\omega^2 + c_L^2 q^2)$  and diverges at low energies and momenta. (In the above estimate, we assume that  $Q$  already reached the RG scale at which  $Q \sim \omega_L \sim c_L \Lambda_0$ , where  $\Lambda_0$  is the UV cutoff, implying that the  $\omega^2 + c_L^2 q^2$  term can be neglected compared to  $\omega_L^2$ .) Thus, the effective Coulomb interaction between electrons becomes highly irrelevant and flows quickly to zero. It means that the Coulomb interaction is effectively screened by the longitudinal

phonon mode. Eventually, the FE critical point is controlled by the following effective field theory:

$$\mathcal{S} = \int d^4x \left[ \sum_{n=1}^N \bar{\psi}_n (Z_\psi \gamma^0 \partial_0 + v_F \gamma^j \partial_j) \psi_n + \frac{1}{2} u_j [-Z_u^2 \partial_0^2 + \omega_T^2 - c_T^2 \nabla^2] P_{jl} u_l + V (u_j P_{jl} u_l)^2 + \lambda \sum_{n=1}^N P_{jl} u_l \bar{\psi}_n \gamma_0 \gamma_j \psi_n \right], \quad (15)$$

where

$$P_{jl}(\mathbf{q}) = \delta_{jl} - q_j q_l / q^2 \quad (16)$$

is the projector to the plane transverse to  $\mathbf{q}$ . The couplings  $V$  and  $\lambda$  here are weakly renormalized after integrating out the longitudinal mode.

Before continuing, we make a remark. We present a low-energy effective theory with the coupling between soft polar phonons and charged fermions given by Eq. (7), which is not a long-range Coulomb interaction. This result is somewhat counterintuitive, as the phonon distortions generate a huge dipolar moment that naïvely induces a long-ranged potential. Consequently, one might expect that the Coulomb interaction between electrons and lattice distortions, arising from a deformation potential, is dominant over the direct coupling (7). However, as we demonstrate above, the Coulomb forces that lead to the strong Fröhlich coupling between electrons and phonons [the third term in Eq. (12)] are also responsible for the generation of huge mass  $\omega_L \propto Q$  for longitudinal phonons [the second term in Eq. (12)] and LO-TO splitting. As a result, the phonon mode that remains soft at the transition is precisely the transverse one, which does not generate a dipolar moment. This result is exact for an isotropic phonon dispersion. In the case of an anisotropic dispersion, there is always a finite mixture between the LO and TO modes leading to a remnant polarization in the soft phonon branch [41]. However, this remnant goes quickly to zero at small  $q$  (as  $q^2$ ), rendering this coupling less relevant than Eq. (7) [48].

## 2. One-loop RG analysis

Now, we analyze the effective field theory for ionic crystals (15) within the one-loop RG approach. To get rid of the exponents  $\eta_\psi$ ,  $\eta_u$ , and  $z$ , which, in principle, can be chosen arbitrary, we focus on the dimensionless quantities which are independent of these engineering dimensions [69,70]. First, we derive coupled RG equations for the ratio of the phonon to electron velocities  $\zeta_T \equiv c_T Z_\psi / v_F Z_u$  and the dimensionless electron-phonon coupling constant  $\beta \equiv \lambda^2 / 4\pi c_T^2 v_F Z_\psi$  (the details of the calculation can be found in Appendixes A and B):



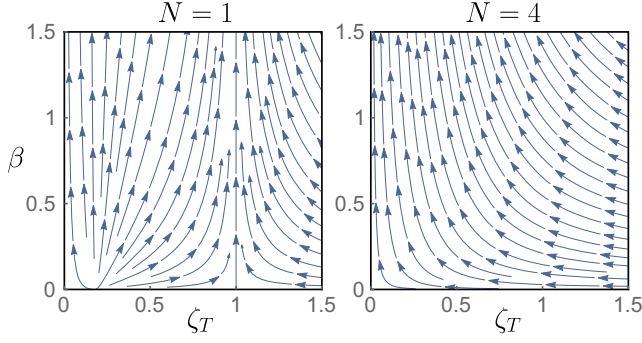


FIG. 4. The RG flow of the dimensionless electron-phonon coupling  $\beta$  and the velocity ratio  $\zeta_T$  given by Eq. (17) for a single Dirac cone (left) and for  $N = 4$  (right). In both cases, the flow is towards strong coupling, where the one-loop RG analysis breaks down.

$$\begin{aligned} \frac{d\zeta_T}{dl} &= -\frac{\zeta_T(1+\zeta_T)^2(1+\zeta_T^2)N - 8\zeta_T^2\beta}{6\pi(1+\zeta_T)^2}\beta, \\ \frac{d\beta}{dl} &= \frac{(1+\zeta_T)^2N - 4(1-\zeta_T)\zeta_T}{3\pi(1+\zeta_T)^2}\beta^2. \end{aligned} \quad (17)$$

The most important result that can be extracted from these equations is that the electron-phonon coupling  $\beta$  flows to the strong-coupling regime; see Fig. 4. Consequently, we conclude that the (3 + 1)D ferroelectric quantum critical point in a Dirac semimetal considered in this paper is generically a strongly coupled problem, even if the original UV value of the coupling constant is small. This conclusion may be contrasted with standard QED in (3 + 1) dimensions, where the flow of the interaction is towards weak coupling, and the low-energy effective theory is the noninteracting Dirac fermion with renormalized parameters [60]. In the next section, we discuss the possible superconducting instabilities resulting from this flow to strong coupling.

Our RG equations are derived under the assumptions of the zero Dirac fermion mass and zero Fermi energy, while the one-loop approximation is valid provided the coupling remains small. Given the flow to the strong coupling, it is important to understand what stops the RG flows. Here, we estimate the scale at which  $\beta$  becomes of the order of 1 and defer the discussion of a finite Dirac mass or Fermi energy to Sec. V. In realistic materials, the Fermi velocity is much bigger than the phonon velocity; thus, one can set  $\zeta_T \approx 0$  in Eq. (17). Then, the equation for the flow of  $\beta$  can be readily integrated. Completely neglecting the mass of the soft mode,  $\omega_T \approx 0$ , we find that  $\beta$  grows to  $O(1)$  at the RG scale  $l_\beta = 3\pi/N\beta_0$ , which corresponds to the momentum scale

$$\Lambda_\beta \sim \Lambda_0 \exp\left(-\frac{3\pi}{N\beta_0}\right). \quad (18)$$

Here,  $\beta_0 \ll 1$  is the initial UV value of the coupling constant at the scale  $\Lambda_0$ .

Another natural scale that serves as a cutoff for our RG equations is set by the flow of the (dimensionless) mass of the transverse phonon mode  $r \equiv \omega_T^2/c_T^2\Lambda_0^2$ , which determines the critical region:

$$\frac{dr}{dl} = r\left(2 + \frac{N\beta}{3\pi}\right) - \frac{4N\beta}{3\pi} + \frac{10\gamma}{3\pi^2}, \quad (19)$$

where  $\gamma \equiv V/c_T^3Z_u$  is the dimensionless phonon-phonon interaction. Assuming that  $\beta$  and  $\gamma$  are small compared to the UV value  $r_0$ , the solution of this equation with the exponential accuracy reads as  $r \sim r_0 e^{2l}$ . The critical regime is determined by the condition  $r \lesssim 1$ , which corresponds to the RG scale  $l_r \approx (1/2)\ln(1/|r_0|)$  or, equivalently, the momentum scale [71]

$$\Lambda_r \sim \Lambda_0 \exp\left[-\frac{1}{2}\ln(1/|r_0|)\right] = \Lambda_0 \sqrt{|r_0|}. \quad (20)$$

If  $\Lambda_\beta > \Lambda_r$ , the theory flows to the strong-coupling regime before the phonon mode gets massive. Our RG equations are applicable then only down to  $\Lambda_\beta$ . In the opposite case,  $\Lambda_r > \Lambda_\beta$ , the RG flow should be stopped at  $\Lambda_r$ , where the transverse phonon mode becomes massive and can be integrated out. At this scale, the system leaves the critical regime, while the coupling between phonons and fermions still remains weak. The corresponding phase diagram is shown in Fig. 5. We consider the latter case in more detail in the next section in the context of superconductivity.

Finally, we discuss the flow of the dimensionless phonon-phonon interaction  $\gamma \equiv V/c_T^3Z_u$ , which corresponds to the anharmonicity of the lattice oscillations:

$$\frac{d\gamma}{dl} = \gamma\left[\frac{N\beta(3-\zeta_T^2)}{6\pi} - \frac{17\gamma}{5\pi^2}\right] - \frac{2N\beta^2\zeta_T}{3}. \quad (21)$$

This equation, again, can be easily analyzed in the physical case  $\zeta_T \approx 0$ . Then, since  $\beta$  is a marginally relevant parameter,  $\gamma$  eventually also flows to strong coupling. It is straightforward to show, however, that this flow does not introduce any new cutoff, as  $\gamma$  can reach the order of 1 no sooner than at  $\Lambda_\beta$  given by Eq. (18); see Fig. 6. This scenario is realized in the large- $N$  limit, i.e., when the term proportional to  $\propto \gamma^2$  on the right-hand side of Eq. (21) can be neglected. It is also interesting to note that sufficiently large  $\zeta_T$  in Eq. (21) can, in principle, drive  $\gamma$  negative, thus indicating a first-order transition into the ferroelectric state. Since we consider  $\zeta_T \sim 1$  hardly realizable in real physical systems, we do not study this possibility in detail here.

Another interesting result that can be inferred from the RG equations is the flow of the electron and phonon velocities (here, we fix the dynamical critical exponent  $z = 1$ ):

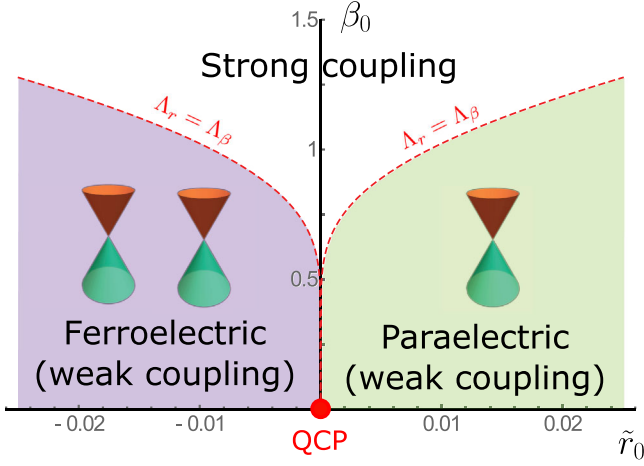


FIG. 5. The phase diagram of a Dirac semimetal with  $N = 4$  close to a ferroelectric quantum critical point as a function of the bare values of the control parameter  $\tilde{r}_0 = r_0 + (5\gamma_0/3\pi^2) - (2N\beta_0/3\pi)$  and the electron-phonon coupling  $\beta_0$ . The red dashed line separates the two regions  $\Lambda_r > \Lambda_\beta$  and  $\Lambda_r < \Lambda_\beta$ , corresponding to weak- and strong-coupling regimes, respectively. In the former region, the finite mass of phonons cuts off the RG flow before  $\beta$  reaches strong coupling, and the theory with renormalized parameters remains weakly coupled. In the latter case,  $\beta$  flows to strong coupling before the system leaves the critical region. This regime is characterized by strong electron-phonon coupling and requires further study. The insets in each region schematically depict the dispersion close to the four  $L$  points. Every Dirac cone in the paraelectric phase splits into two Weyl points in the ferroelectric phase.

$$\begin{aligned} \frac{d(v_F/Z_\psi)}{dl} &= -\frac{4\zeta_T\beta}{3\pi(1+\zeta_T)^2} \frac{v_F}{Z_\psi}, \\ \frac{d(c_T/Z_u)}{dl} &= -\frac{(1+\zeta_T^2)\beta N}{6\pi} \frac{c_T}{Z_u}. \end{aligned} \quad (22)$$

We see that one of the physical properties of the ferroelectric critical point in Dirac materials is the reduction of

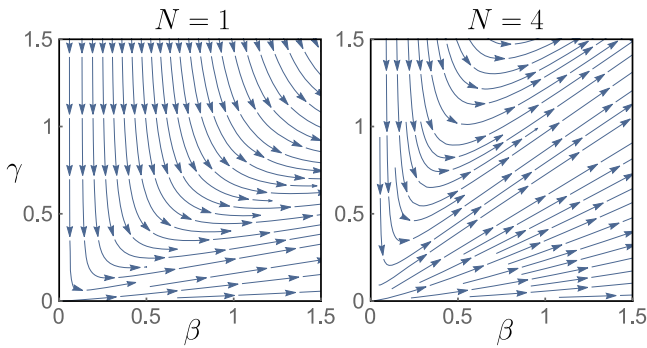


FIG. 6. The RG flow of the dimensionless phonon-phonon coupling  $\gamma$  and the dimensionless electron-phonon coupling  $\beta$  corresponding to Eqs. (17) and (21) in the limit  $\zeta_T = 0$ . The left represents the case of a single fermionic flavor  $N = 1$ , and the right is for  $N = 4$ . The scale when  $\gamma$  reaches the order of 1 never exceeds  $\Lambda_\beta$ .

the velocities under the RG for both the transverse phonon modes and the Dirac fermions. Furthermore, as is shown in Fig. 4, for  $N = 1$ , the velocity ratio  $\zeta_T$  flows to one of two possible values  $\zeta_0 = 0$  or  $\zeta_1 = 1$ , depending on whether the initial value of  $\zeta_T$  is smaller or larger than  $\zeta_m = t/3^{2/3} - 2/(3^{1/3}t) - 1 \approx 0.18$ , respectively, with  $t = (18 + 2\sqrt{87})^{1/3}$ . If  $N > 1$ , the flow is always towards  $\zeta_0 = 0$ .

So far, we consider only a rotationally symmetric model with isotropic electron and phonon velocities. For  $N > 1$ , however, there is no symmetry that forbids anisotropic terms which manifest the symmetry of the underlying lattice. Nevertheless, accounting for these terms does not modify the main qualitative results described above. Hence, we focus on the isotropic case for the rest of the paper, for simplicity, and defer the discussion of possible anisotropies to Appendix D.

## B. Covalent crystals ( $Q = 0$ )

Now we perform similar RG analysis for covalent crystals, exemplified by elemental bismuth. The “ferroelectric” phase in these materials is characterized by broken inversion symmetry but not by a spontaneous dipolar moment of the lattice, because the optical phonon distortion  $\mathbf{u}$  generates a negligible amount of polarization in covalent crystals.

While the main qualitative results, such as the flow to strong coupling, in this case are the same as for ionic crystals, certain important differences should be discussed. In particular, the absence of lattice polarization implies that the effective theory for covalent crystals is given by Eq. (8) with  $Q = 0$ . As a result of this important difference, the argumentation of Sec. IV A about the screening of Coulomb interaction by massive longitudinal phonons no longer holds. Instead, one should keep track of the flows of the parameters  $\varepsilon_\infty$  and  $e$ , in addition to those considered in Eq. (17). Focusing again on dimensionless parameters that do not depend on engineering dimensions  $\eta_\psi, \eta_u, \eta_\phi$ , and  $z$ , we find the following set of coupled one-loop RG equations:

$$\begin{aligned} \frac{d\beta}{dl} &= \frac{N\beta^2}{3\pi} + \frac{4\beta^2\zeta_T(\zeta_T - 1)}{3\pi(1+\zeta_T)^2} - \frac{2\beta^2\zeta_T^2}{\pi\zeta_L(1+\zeta_L)^2}, \\ \frac{d\alpha}{dl} &= -\frac{2(N+1)\alpha^2}{3\pi} + \frac{4\alpha\beta\zeta_T}{3\pi(1+\zeta_T)^2} + \frac{2\alpha\beta\zeta_T^2(3+\zeta_L)}{3\pi\zeta_L(1+\zeta_L)^2}, \\ \frac{d\zeta_T}{dl} &= -\frac{N\beta(1+\zeta_T^2)\zeta_T}{6\pi} + \frac{4\beta\zeta_T^2}{3\pi(1+\zeta_T)^2} \\ &\quad + \frac{2\beta\zeta_T^3(3+\zeta_L)}{3\pi\zeta_L(1+\zeta_L)^2} - \frac{2\alpha\zeta_T}{3\pi}, \\ \frac{d\zeta_L}{dl} &= \frac{N\beta\zeta_T^2(1-\zeta_L^2)}{6\pi\zeta_L} + \frac{4\beta\zeta_T\zeta_L}{3\pi(1+\zeta_T)^2} \\ &\quad + \frac{2\beta\zeta_T^2(3+\zeta_L)}{3\pi(1+\zeta_L)^2} - \frac{2\alpha\zeta_L}{3\pi}, \end{aligned} \quad (23)$$

where we define  $\beta \equiv \lambda^2/4\pi v_F c_T^2 Z_\psi$ ,  $\alpha \equiv e^2/\epsilon_\infty v_F Z_u$ ,  $\zeta_T \equiv c_T Z_\psi/v_F Z_u$ , and  $\zeta_L \equiv c_L Z_\psi/v_F Z_u$ .

Since both the longitudinal and the transverse phonon modes become massless at the transition in covalent crystals, they should be treated on equal footing. Consequently, one could, in principle, consider two (not independent) dimensionless couplings  $\beta = \lambda^2/4\pi v_F c_T^2 Z_\psi$  and  $\tilde{\beta} = \lambda^2/4\pi v_F c_L^2 Z_\psi$ , which quantify the electron-electron interaction strength mediated by the transverse phonons and the longitudinal phonons, respectively. It is straightforward to show, however, that, in the physical limit  $\zeta_T \sim \zeta_L \ll 1$ ,  $\tilde{\beta}$  is marginally irrelevant, while  $\beta$  flows to strong coupling. Indeed, in this limit, first two equations in Eq. (23) take the form (assuming also that  $\beta\zeta_T \ll \alpha$ )

$$\begin{aligned} \frac{d\beta}{dl} &= \frac{N\beta^2}{3\pi}, \\ \frac{d\alpha}{dl} &= -\frac{2(N+1)\alpha^2}{3\pi}, \end{aligned} \quad (24)$$

while the analogous equation for  $\tilde{\beta}$  would read as

$$\frac{d\tilde{\beta}}{dl} = -\frac{N\tilde{\beta}^2}{3\pi}. \quad (25)$$

We note that, in this limit, the renormalization of the fine structure constant  $\alpha$  is identical to that in standard QED in  $(3+1)$  dimensions [59,60]. Similarly to the case of ionic crystals, electron-phonon coupling  $\beta$  flows to the strong-coupling regime, while the Coulomb interaction  $\alpha$  becomes suppressed under the RG. The important difference, however, is that now  $\alpha$  is only marginally irrelevant and flows to zero much slower. The reason for this difference is that the Coulomb screening in covalent crystals is due to interband (between particle and hole bands) transitions, which is much weaker than the screening by the lattice polarization in ionic crystals.

The flow of the phonon velocities can also be easily studied in the limit  $\zeta_T \sim \zeta_L \ll 1$ . Analogously to ionic crystals,  $\zeta_T$  flows to zero in this regime. The flow of  $\zeta_L$ , on the other hand, is sensitive to the number of flavors  $N$  and to the initial conditions, as well as to the scale that stops the RG. For instance, at sufficiently large  $N$ ,  $\zeta_L$  is increased under the RG.

Finally, the flows of the phonon-phonon coupling  $\gamma$  and the phonon mass  $r$  are qualitatively similar to the case of ionic crystals, so we do not consider them in detail here.

## V. SUPERCONDUCTIVITY

In the previous section, we analyze the RG flow of the electron-phonon coupling near a ferroelectric quantum critical point. We find that, generically, the critical point is unstable and flows to strong electron-phonon coupling, while the Coulomb interaction flows to weak coupling.

As a result, we anticipate that the effective electron-electron attraction mediated by the ferroelectric phonon modes will become dominant over the Coulomb repulsion. Hence, the natural next step in our work is to apply this result to study superconductivity.

We emphasize that in our scenario, for both ionic and covalent crystals, the enhancement of the attractive interaction over the Coulomb repulsion does not require a finite electron density, in contrast to the Anderson-Morel theory. Nonetheless, this does not imply that the superconducting transition temperature does not depend on the density. At least at weak coupling,  $\beta \lesssim 1$ , a finite density of states is essential to obtain a finite  $T_c$ . Therefore, we now relax our previous assumption about the Fermi energy exactly at the Dirac point and assume a nonzero Fermi momentum  $k_F$ . As before, we separately consider the cases of ionic and covalent crystals. We also focus on the paraelectric side of the transition, i.e., consider systems possessing both time-reversal and inversion symmetries in the normal state.

### A. Ionic crystals

As we show in Sec. IV, one can define two scales  $\Lambda_\beta$  and  $\Lambda_r$  given by Eqs. (18) and (20), which correspond to the divergence of the electron-phonon coupling  $\beta$  and the phonon mass  $r$ , respectively. When  $\Lambda_r > \Lambda_\beta$ ,  $r$  diverges first, and the flow is terminated before  $\beta$  reaches strong coupling (this regime is denoted by the shaded regions in Fig. 5). In what follows, we consider this weak-coupling limit, where the BCS approach is applicable, and leave the strong-coupling scenario  $\Lambda_\beta > \Lambda_r$  for a future work.

The additional scale we introduce,  $k_F$ , can, in principle, also put the flow to a halt when the running scale  $\Lambda(l) = \Lambda_0 \exp(-l)$  becomes of the order of  $k_F$ . Thus, depending on the ratio between  $k_F$  and  $\Lambda_r$ , one may again consider two cases. The first case,  $k_F \gtrsim \Lambda_r$ , is close to the standard Anderson-Morel scenario with the phonon-associated scale  $(\omega_T/c_T)|_{l=0}$  being smaller than  $k_F$ , and we do not consider it here in detail. Since we are interested in understanding superconductivity at a very low density, we focus on the opposite limit  $\Lambda_r \gtrsim k_F$ . In this case, the screening of the Coulomb repulsion by longitudinal phonons occurs well above the Fermi scale, as discussed below Eq. (14), and we obtain a Fermi liquid with *static* phonon-mediated attraction. The inequality  $\Lambda_r \gtrsim k_F$  also implies that (at a finite density) the system is away from the immediate vicinity of the critical point; the behavior exactly at criticality will be considered in a separate work.

To obtain an effective low-energy interaction, we allow the system to flow according to the RG equations derived in Sec. IV A until it reaches the scale  $\Lambda_r$ . We then use Eq. (15) to integrate out the transverse phonon mode, which is massive at this scale, with the effective propagator that can be considered frequency and momentum independent. This procedure results in the attractive interaction Hamiltonian

$$\mathcal{H}_{\text{FE}} = -\frac{2\pi v_F^* \beta^*}{\Lambda_0^2} \sum_{k, k', q} P_{jl}(\mathbf{q}) (\psi_{k+q}^\dagger \gamma_j \psi_k) (\psi_{k'-q}^\dagger \gamma_l \psi_{k'}), \quad (26)$$

where the effective interaction constant

$$\beta^* \equiv \beta(l_r) = \frac{\beta_0}{1 - \frac{\beta_0 N}{3\pi} \log \frac{\Lambda_0}{\Lambda_r}} \quad (27)$$

is obtained from Eq. (17) in the limit of  $\zeta_T \ll 1$ , and we also define the renormalized Fermi velocity  $v_F^* \equiv v_F(l_r)$ . To make the analysis similar to the conventional BCS at this point, we write Eq. (26) in the Hamiltonian formalism (and use  $\psi^\dagger$  instead of  $\bar{\psi}$ ). We also note that the static interaction, Eq. (26), becomes a good approximation below the scale  $\Lambda_r$ , where  $\omega \lesssim \omega_T$ , similar to BCS theory.

### 1. Projection onto the Fermi level

Now we analyze the superconducting instabilities due to interaction (26). We assume that the Fermi energy  $\varepsilon_F = v_F k_F$  is much larger than the superconducting gap,  $\varepsilon_F \gg \Delta$ ; hence, the conventional weak-coupling BCS-like treatment is applicable. In this case, it is convenient to project all operators onto the band where the Fermi level resides, thus significantly simplifying the model by reducing it from the original four-orbital to an effective two-orbital. In the paraelectric phase, the only case we consider in this section, both time-reversal and inversion symmetry are present in the normal state; hence, all energy bands remain double degenerate even in the presence of strong spin-orbit coupling. The electron states are characterized by a two-component spinor  $c_k = [c_1(\mathbf{k}), c_2(\mathbf{k})]^T$ . In the presence of spin-orbit coupling, however, components  $c_{1,2}$  are not spin eigenstates anymore but rather eigenstates in some band basis. The choice of this basis is not unique. For concreteness, we choose the so-called manifestly covariant Bloch basis (MCBB), in which  $[c_1(\mathbf{k}), c_2(\mathbf{k})]^T$  transforms as an ordinary  $SU(2)$  spin-1/2 [57]. To find this basis, we diagonalize the Hamiltonian which corresponds to Eq. (2) and choose the band eigenstates to be fully spin polarized along the  $z$  axis at the origin of the point group symmetry operations (see also Refs. [58,72] for more details). The eigenvectors  $b_1(\mathbf{k})$  and  $b_2(\mathbf{k})$  in the MCBB that correspond to the states near Fermi energy are given, respectively, by

$$b_1(\mathbf{k}) = \frac{1}{2} \begin{pmatrix} \eta - \hat{k}_z \\ -\hat{k}_+ \\ \eta + \hat{k}_z \\ \hat{k}_+ \end{pmatrix}, \quad b_2(\mathbf{k}) = \frac{1}{2} \begin{pmatrix} -\hat{k}_- \\ \eta + \hat{k}_z \\ \hat{k}_- \\ \eta - \hat{k}_z \end{pmatrix}, \quad (28)$$

where  $\eta = \pm 1$  corresponds to the conduction and valence bands, respectively, and we define  $\hat{k}_\pm = (k_x \pm ik_y)/k$ . The mapping onto the MCBB then simply implies the

transformation  $\psi(\mathbf{k}) \rightarrow b_1(\mathbf{k})c_1(\mathbf{k}) + b_2(\mathbf{k})c_2(\mathbf{k})$  and can schematically be written as  $\psi(\mathbf{k}) = \mathcal{Q}_\eta(\mathbf{k})c(\mathbf{k})$ , where  $\mathcal{Q}_\eta(\mathbf{k})$  is a projector onto the MCBB. It is straightforward to show then that the Dirac bilinear  $\gamma_j$ , which couples to a soft phonon mode, projects onto

$$M_{p,\mathbf{k}}^j = \mathcal{Q}_\eta^\dagger(\mathbf{p}) \gamma_j \mathcal{Q}_\eta(\mathbf{k}) = \frac{\eta}{2} [i(\hat{p}_j - \hat{k}_j) + (\hat{k}_l + \hat{p}_l) \sigma_m \epsilon_{lmj}], \quad (29)$$

where  $\epsilon_{lmj}$  is the Levi-Civita tensor,  $\sigma_j$  here are Pauli matrices acting in the MCBB, and we define  $\hat{k}_j \equiv k_j/k$ .

The effective interaction (26) projected onto the band with the Fermi level has the form (here, we use the notation  $\hat{\mathbf{k}} \equiv \mathbf{k}/k$ )

$$\begin{aligned} \mathcal{H}_{\text{FE}}^T \simeq & -\frac{\pi v_F^* \beta^*}{2\Lambda_0^2} \sum_{k, k', q} P_{jl}(\mathbf{q}) \{ c_{k+q}^\dagger [i(\widehat{\mathbf{k}} + \mathbf{q} - \hat{\mathbf{k}}) \\ & + (\hat{\mathbf{k}} + \widehat{\mathbf{k}} + \mathbf{q}) \times \boldsymbol{\sigma}]_j c_k \} \times \{ c_{k'-q}^\dagger [i(\widehat{\mathbf{k}}' - \mathbf{q} - \hat{\mathbf{k}}') \\ & + (\hat{\mathbf{k}}' + \widehat{\mathbf{k}}' - \mathbf{q}) \times \boldsymbol{\sigma}]_l c_{k'} \}. \end{aligned} \quad (30)$$

### 2. Pairing channels and transition temperature

To demonstrate the superconducting instabilities, we now decompose interaction (30) into pairing channels, analogously to how it is done in Ref. [58]. The time-reversal invariant superconducting order parameter generally takes the form

$$\hat{F}^\dagger = \sum_{k, \alpha\beta\gamma} \epsilon_{\beta\gamma} F_{\alpha\beta}(\mathbf{k}) c_{k\alpha}^\dagger c_{-k\gamma}^\dagger, \quad (31)$$

where, again,  $\epsilon_{\beta\gamma}$  is the Levi-Civita symbol. In systems with strong spin-orbit coupling, spin  $S$  and orbital angular momentum  $L$  are not good quantum numbers. Instead, in systems with  $O(3)$  symmetry considered here, all possible orders are characterized by the total angular momentum  $J = L + S$ . As is shown in Refs. [57,58], the form factors  $F_{\alpha\beta}(\mathbf{k})$  up to the order of  $J = 1$  have the form shown in Table II.  $L = 0$  state  $F_0$  corresponds to the conventional  $s$ -wave pairing with  $J = 0$ , while  $L = 1$  states are odd-parity

TABLE II. The decomposition of the phonon-mediated interactions (30) and (38) into the BCS channels  $F_n$  with total angular momentum  $J = 0$  ( $a_0$  and  $a_1$ ) and  $J = 1$  ( $a_2$ ); see Eqs. (32) and (40). Positive coefficients  $a_i$  imply the attraction in the corresponding BCS channels.

Form factor	$\mathcal{P}$	Coefficient	Transverse	Longitudinal
$F_0(\mathbf{k}) = I$	Even	$a_0$	1	2
$F_1(\mathbf{k}) = \hat{\mathbf{k}} \cdot \boldsymbol{\sigma}$	Odd	$a_1$	-1	-2
$F_2^j(\mathbf{k}) = (\hat{\mathbf{k}} \times \boldsymbol{\sigma})^j$	Odd	$a_2$	1/2	-3/2

$p$  wave and transform as a pseudoscalar ( $F_1$  with  $J = 0$ ) and a vector ( $F_2^j$  with  $J = 1$ ) under the symmetry operations.

Next, we restrict the effective interaction (30) to the Cooper channel with the zero total momentum by keeping terms with  $\mathbf{k}' = -\mathbf{k}$  only. Focusing on the states near the Fermi surface,  $|\mathbf{k}| \approx |\mathbf{k}'| \approx |\mathbf{k} + \mathbf{q}| \approx |\mathbf{k}' - \mathbf{q}| \approx k_F$ , it is straightforward to decompose Eq. (30) into the pairing channels  $F_n$  [58]:

$$\mathcal{H}_{\text{FE}}^T \approx -\frac{\pi v_F^* \beta^*}{2\Lambda_0^2} \sum_{n=0}^2 a_n^T \sum_j \hat{F}_n^{j\dagger} \hat{F}_n^j + \dots, \quad (32)$$

where coefficients  $a_n^T$  are listed in Table II. The ellipsis on the right-hand side in Eq. (32) denotes terms with  $J > 1$  [73]. The contribution from these terms is numerically small, and we do not consider it in this paper.

Up to the order of  $J = 1$ , only two channels are attractive and lead to a superconducting instability: the scalar  $\hat{F}_0$  with  $a_0^T = 1$  and the vector  $\hat{F}_2^j$  with  $a_2^T = 1/2$ . We thus conclude that pairing in the  $s$ -wave channel is the most dominant superconducting instability.

The transition temperature  $T_c$  (for a given  $n$ ) can be estimated from Eq. (32) using the usual gap equation [74]:

$$\delta_{ij} = \frac{\pi v_F^* \beta^*}{2\Lambda_0^2} a_n^T \sum_k \text{tr}[F_n^i(\mathbf{k}) F_n^j(\mathbf{k})] \frac{\tanh(\xi_k/2T_c)}{\xi_k}. \quad (33)$$

In the case of the most attractive  $s$ -wave channel, it takes the form

$$1 \approx \frac{2\pi v_F^* \beta^* a_0^T \nu^*}{\Lambda_0^2} \int_{\sim T_c}^{\sim \varepsilon_F} \frac{d\xi}{\xi}, \quad (34)$$

where  $\nu^* = k_F^2(l_r)/2\pi^2 v_F(l_r)$  is the density of states at the Fermi energy per one spin projection per one Dirac node, with all quantities entering it taken at the RG scale  $l_r$ . We emphasize that the upper cutoff in Eq. (33) is not the phonon frequency, as in the standard BCS theory, but given by the Fermi energy. This situation is somewhat analogous to the superfluidity in a charge-neutral Fermi liquid, studied in Ref. [75]. We estimate the transition temperature from Eq. (33) as

$$\begin{aligned} T_c &\sim \varepsilon_F \exp\left(-\frac{\Lambda_0^2}{2\pi v_F^* \beta^* a_0^T \nu^*}\right) \\ &= \varepsilon_F \exp\left(-\frac{\pi \Lambda_r^2}{k_F^2 \beta^*}\right) = \varepsilon_F \exp\left(-\frac{\pi \omega_{T0}^2}{k_F^2 c_{T0}^2 \beta^*}\right). \end{aligned} \quad (35)$$

The parameters  $k_F$ ,  $c_{T0}$ , and  $\omega_{T0}$  in this equation are the original (UV) values of the Fermi momentum, phonon velocity, and phonon mass, respectively, while  $\beta_*$  is renormalized according to Eq. (27), and we use  $k_F(l) = k_F e^l$ .

In particular,  $k_F$  is related to the total electron density  $n_0$  and the number of Dirac nodes  $N$  as  $k_F = (3\pi^2 n_0/N)^{1/3}$ . We see that the proximity to the ferroelectric critical point leads to a significant enhancement of  $T_c$ . To emphasize this point, we rewrite Eq. (35) in the form

$$T_c \sim T_{c0} \left(\frac{1}{r_0}\right)^\delta \gg T_{c0}, \quad \delta = \frac{N \omega_{T0}^2}{6k_F^2 c_{T0}^2} \gg 1, \quad (36)$$

where  $T_{c0} \sim \varepsilon_F \exp(-\pi \omega_{T0}^2 / k_F^2 c_{T0}^2 \beta_0)$  is the estimate for a transition temperature that we would obtain without taking into account the critical nature of the ferroelectric fluctuations. We see that, even within the weak-coupling approximation  $\beta_0 \ln(\Lambda_0/\Lambda_r) \lesssim 1$ , we obtain a huge enhancement of the transition temperature by a factor of  $(1/r_0)^\delta$  due to the renormalization of the coupling  $\beta$ . This result is to some extent similar to the enhancement of  $T_c$  by the critical nematic fluctuations obtained in Ref. [29].

We see from Eq. (35) that the transition temperature is exponentially sensitive to  $\beta^*$  and  $k_F/\Lambda_r$ , both of which can be made of the order of 1 close to the FE QCP. We estimate the magnitude of  $T_c$  given by Eq. (35) using parameters of a realistic system, such as  $\text{Pb}_{1-x}\text{Sn}_x\text{Te}$ . We assume that the system is close enough to the QCP such that  $\beta^*$  gets sufficiently renormalized and becomes of the order of one [in particular, we take  $\beta^* = 1$ , which is controlled by the logarithmic divergence in Eq. (27)]. The phonon velocity can be estimated as  $c_{T0} = 3 \times 10^3$  m/s [76,77], and we take a small (since we are close to the critical point) phonon mass  $\omega_{T0} = 0.35$  meV. The low-energy electronic structure of  $\text{Pb}_{1-x}\text{Sn}_x\text{Te}$  is given by  $N = 4$  Dirac cones with a typical Fermi velocity  $v_F \approx 10^6$  m/s [78]. For the electron density  $n_0 = 2 \times 10^{17}$  cm $^{-3}$ , we find from Eq. (35)  $T_c \approx 440$  mK with  $\varepsilon_F \approx 870$  K and  $k_F/\Lambda_r \approx 0.64$ . Analogously, for  $n_0 = 4 \times 10^{17}$  cm $^{-3}$ , we obtain  $T_c \approx 9.1$  K with  $\varepsilon_F \approx 1100$  K and  $k_F/\Lambda_r \approx 0.81$ . Despite the fact that the values of  $T_c$  obtained above are only very rough estimates, we conclude that Eq. (35) may lead to a significant transition temperature even for a very low density of electrons. The direct electron-phonon coupling Eq. (7), which remains finite at zero momentum, is a prerequisite for this result. It leads to a phonon-mediated interaction with typical range  $\Lambda_r^{-1}$ , which, sufficiently close to the critical point, becomes of the same order as the interparticle distance  $k_F^{-1}$ . This is in perfect agreement with the result by Gurevich, Larkin, and Firsov [14], who point out that low-density superconductivity necessarily requires a sufficiently long-ranged attractive interaction.

Finally, we estimate the temperature that would correspond to a transition into the  $p$ -wave superconducting state  $T_{cp}$ :

$$T_{cp} \sim \varepsilon_F \exp\left(-\frac{3\Lambda_0^2}{4\pi v_F^* \tilde{\beta}^* a_2^T v^*}\right) = \varepsilon_F \exp\left(-\frac{3\pi\omega_{T0}^2}{k_F^2 c_{T0}^2 \beta^*}\right). \quad (37)$$

An additional factor of 3/2 in the exponent appears due to the averaging over the directions of vector  $\mathbf{k}$  in Eq. (33).  $T_{cp}$  is exponentially smaller than  $T_c$ , and, consequently, the  $p$ -wave superconducting phase seems unreachable within the present scenario. However, we demonstrate in the next section that the presence of the repulsive Coulomb interaction can, under certain conditions, suppress the  $s$ -wave channel and drive a system into the odd-parity  $p$ -wave superconducting state.

## B. Covalent crystals

Our analysis of superconductivity in covalent crystals is similar to the ionic case. There are, however, two important differences. First, the longitudinal phonon mode also becomes soft at a ferroelectric transition, and, consequently, there will be an additional contribution to the effective electron-electron interaction mediated by a longitudinal mode. Second, the Coulomb repulsion is not screened by the lattice polarization but only by the interband transitions. Consequently, as we show in Sec. IV B, the correspondent coupling constants  $\tilde{\beta}$  and  $\alpha$  are marginally irrelevant; see Eqs. (24) and (25). They flow to zero only logarithmically upon RG and, thus, should be taken into account in the weak-coupling regime we are considering here. As we show below in Sec. V B 1, the inclusion of the Coulomb interaction allows one, upon proper tuning of the coupling constants, to realize a  $p$ -wave superconductor.

The effective electron-electron interaction due to longitudinal phonons projected onto the Fermi level has the same form as Eq. (26), but with the substitution  $P_{ij}(\mathbf{q}) \rightarrow \delta_{ij} - P_{ij}(\mathbf{q})$  and  $\beta^* \rightarrow \tilde{\beta}^*$ :

$$\begin{aligned} \mathcal{H}_{\text{FE}}^L \simeq & -\frac{\pi v_F^* \tilde{\beta}^*}{2\Lambda_0^2} \sum_{\mathbf{k}, \mathbf{k}', \mathbf{q}} [\delta_{jl} - P_{jl}(\mathbf{q})] \\ & \times \{c_{\mathbf{k}+\mathbf{q}}^\dagger [i(\widehat{\mathbf{k}} + \widehat{\mathbf{q}} - \widehat{\mathbf{k}}) + (\widehat{\mathbf{k}} + \widehat{\mathbf{k}} + \widehat{\mathbf{q}}) \times \boldsymbol{\sigma}]_j c_{\mathbf{k}}\} \\ & \times \{c_{\mathbf{k}'-\mathbf{q}}^\dagger [i(\widehat{\mathbf{k}}' - \widehat{\mathbf{q}} - \widehat{\mathbf{k}}') + (\widehat{\mathbf{k}}' + \widehat{\mathbf{k}}' - \widehat{\mathbf{q}}) \times \boldsymbol{\sigma}]_l c_{\mathbf{k}'}\}, \end{aligned} \quad (38)$$

where  $\tilde{\beta}^*$  is given by [see Eq. (25)]

$$\tilde{\beta}^* \equiv \tilde{\beta}(l_r) = \frac{\beta_0}{1 + \frac{\beta_0 N}{3\pi} \log \frac{\Lambda_0}{\Lambda_r}}, \quad (39)$$

and, again, we use the notation  $\hat{\mathbf{k}} \equiv \mathbf{k}/k$ . The decomposition into the pairing channels has a form similar to Eq. (32), with  $\beta^*$  substituted by  $\tilde{\beta}^*$ :

$$\mathcal{H}_{\text{FE}}^L \approx -\frac{\pi v_F^* \tilde{\beta}^*}{2\Lambda_0^2} \sum_{n=0}^2 a_n^L \sum_j \hat{F}_n^{j\dagger} \hat{F}_n^j + \dots, \quad (40)$$

and coefficients  $a_n^L$  are listed in Table II.

We see that the interaction mediated by the longitudinal phonons also favors  $s$ -wave pairing; hence, its only effect is to modify the expression for  $T_c$  accordingly. The inclusion of the Coulomb interaction, on the other hand, may have more dramatic consequences, leading, under certain conditions, to the  $p$ -wave superconductivity in covalent crystals.

### 1. Possibility of $p$ -wave pairing

To demonstrate how the Coulomb repulsion may result in the  $p$ -wave superconductivity, we generalize our analysis for the case of a finite Dirac mass  $m$  in Eq. (2). Again, we focus on the regime with  $m/v_F, k_F \lesssim \Lambda_r$ , so the RG flow is not affected by the nonzero mass or Fermi energy and stops at the same scale  $\Lambda_r$ , while the ratio  $m/v_F k_F$  can be arbitrary.

In the case of a finite mass, the eigenvectors in the MCBB (28) are generalized as

$$b_1(\mathbf{k}) = \begin{pmatrix} \beta_+ - \beta_- \hat{k}_z \\ -\beta_- \hat{k}_+ \\ \beta_+ + \beta_- \hat{k}_z \\ \beta_- \hat{k}_+ \end{pmatrix}, \quad b_2(\mathbf{k}) = \begin{pmatrix} -\beta_- \hat{k}_- \\ \beta_+ + \beta_- \hat{k}_z \\ \beta_- \hat{k}_- \\ \beta_+ - \beta_- \hat{k}_z \end{pmatrix}, \quad (41)$$

where we consider only states at the Fermi surface,  $|\mathbf{k}| = k_F$ , and define  $\beta_\pm = (1/2)\sqrt{1 \pm m/\varepsilon_F}$  with  $\varepsilon_F = \sqrt{m^2 + v_F^2 k_F^2}$ . Equation (41) also assumes the Fermi energy inside the electron band, while the expression for the opposite case is obtained by the substitution  $\beta_- \rightarrow \beta_+, \beta_+ \rightarrow -\beta_-$ . Hereafter, all quantities entering the equations (e.g., Fermi velocity  $v_F$ , Fermi momentum  $k_F$ , mass  $m$ , Fermi energy  $\varepsilon_F$ , Thomas-Fermi vector  $q_{\text{TF}}$ , or density of states  $\nu$ ) are meant to be taken at the RG scale  $l_r$  (which corresponds to  $\Lambda_r$  in momentum space), and we suppress index  $*$  for brevity, unless otherwise specified.

The effect of a finite mass on the phonon-mediated part of the interaction is rather simple: It results in the extra prefactor  $v_F^2 k_F^2 / \varepsilon_F^2$  in Eqs. (30) and (38). As a result, all coefficient  $a_n^L$  in Eq. (32) should be replaced by  $a_n^T \rightarrow (v_F^2 k_F^2 / \varepsilon_F^2) a_n^T$  [and analogously for all coefficients  $a_n^L$  in Eq. (40)]. Finally, the density of states  $\nu$  in Eqs. (35) and (37) should be modified according to  $\nu = \varepsilon_F k_F / 2\pi^2 v_F^2$ .

The decomposition of the Coulomb repulsion is more subtle. Because of its long-range nature, the momentum dependence of the interaction must also be taken into

account. Taking the simple Thomas-Fermi approximation and projecting onto the MCBB, we find

$$\begin{aligned} \mathcal{H}_C &= 8\pi\alpha^* v_F \sum_{\mathbf{k}, \mathbf{p}, \mathbf{q}} \frac{1}{q^2 + q_{\text{TF}}^2} \\ &\times \{c_{\mathbf{k}+\mathbf{q}}^\dagger [(\beta_+^2 + \beta_-^2 (\widehat{\mathbf{k}+\mathbf{q}} \cdot \widehat{\mathbf{k}})) + i\beta_-^2 \widehat{\mathbf{k}+\mathbf{q}} \times \widehat{\mathbf{k}} \cdot \boldsymbol{\sigma}] c_{\mathbf{k}}\} \\ &\times \{c_{\mathbf{k}'-\mathbf{q}}^\dagger [(\beta_+^2 + \beta_-^2 (\widehat{\mathbf{k}'-\mathbf{q}} \cdot \widehat{\mathbf{k}'}) + i\beta_-^2 \widehat{\mathbf{k}'-\mathbf{q}} \times \widehat{\mathbf{k}'} \cdot \boldsymbol{\sigma}] c_{\mathbf{k}'}\}, \end{aligned} \quad (42)$$

where  $q_{\text{TF}}^2 = 8\pi N\alpha^* v_F$  is the square of the Thomas-Fermi wave vector and  $\alpha^*$  is given by

$$\alpha^* \equiv \alpha(l_r) = \frac{\alpha_0}{1 + \frac{2(N+1)}{3\pi} \alpha_0 \log \frac{\Lambda_0}{\Lambda_r}}. \quad (43)$$

Again, all quantities entering  $q_{\text{TF}}$  here are taken at the RG scale  $l_r$ .

Focusing on the states at the Fermi surface only, we decompose the Coulomb interaction (42) into the pairing channels:

$$\mathcal{H}_C \approx \frac{\pi\alpha^* v_F}{k_F^2} \sum_{n=0}^2 f_n \left( \frac{q_{\text{TF}}}{k_F} \right) \sum_j \hat{F}_n^{j\dagger} \hat{F}_n^j + \dots, \quad (44)$$

where the ellipsis stands for the terms with  $J > 1$  which we neglect here. The expression for functions  $f_n(x)$  are rather cumbersome and presented in Appendix E.

Summing up contributions from the transverse and longitudinal phonon modes, Eqs. (32) and (40), and direct Coulomb repulsion (44), the decomposition of the total effective electron-electron interaction into the pairing channels has the form

$$\begin{aligned} \mathcal{H}_{\text{FE}}^T + \mathcal{H}_{\text{FE}}^L + \mathcal{H}_C &\approx \pi v_F \sum_{n=0}^2 \left[ -a_n^T \frac{\beta^* v_F^2 k_F^2}{2\Lambda_0^2 \varepsilon_F^2} - a_n^L \frac{\tilde{\beta}^* v_F^2 k_F^2}{2\Lambda_0^2 \varepsilon_F^2} \right. \\ &\left. + \frac{\alpha^*}{k_F^2} f_n \left( \frac{q_{\text{TF}}}{k_F} \right) \right] \sum_j \hat{F}_n^{j\dagger} \hat{F}_n^j + \dots, \end{aligned} \quad (45)$$

where coefficients  $a_n^T$  and  $a_n^L$  are presented in Table II and functions  $f_n(x)$  are listed in Appendix E. Equation (45) is a direct generalization of Eq. (32) for the case of covalent crystals and a finite Dirac mass. The expressions for  $T_c$  in the attractive pairing channels can also be easily generalized for this case.

In general, functions  $f_n(x)$  have a rather complicated form. However, to demonstrate how the  $p$ -wave superconductivity may appear, it is sufficient to consider the limit of a very low density,  $v_F k_F \ll \varepsilon_F = \sqrt{m^2 + v_F^2 k_F^2}$ . Assuming further that  $\alpha^*$  is not too small, we find

$$\begin{aligned} f_0 \left( \frac{q_{\text{TF}}}{k_F} \right) &\approx \frac{\pi}{4N\alpha^*} \frac{v_F k_F}{\varepsilon_F}, \\ f_1 \left( \frac{q_{\text{TF}}}{k_F} \right) &\approx \frac{\pi^2}{24N^2 \alpha^{*2}} \left( \frac{v_F k_F}{\varepsilon_F} \right)^2, \\ f_2 \left( \frac{q_{\text{TF}}}{k_F} \right) &\approx \frac{\pi^2}{16N^2 \alpha^{*2}} \left( \frac{v_F k_F}{\varepsilon_F} \right)^2. \end{aligned} \quad (46)$$

It is clear from the above expression that, as long as  $\alpha^* \varepsilon_F \gg v_F k_F$ , the  $s$ -wave channel is much more suppressed by the Coulomb repulsion than the  $p$ -wave channel,  $f_0 \gg f_{1,2}$ . We further assume that the coupling constants  $\beta^*$  and  $\tilde{\beta}^*$  are renormalized significantly enough, such that  $\beta^* \sim 1$  and  $\tilde{\beta}^* \approx 0$ . It means that the system is on the verge of entering the strong-coupling regime, while the contribution from the interaction mediated by the longitudinal phonons can be neglected. Then, the ratio between the phonon-mediated attraction and the Coulomb repulsion in the  $s$ -wave channel can be rudely estimated as

$$|\mathcal{H}_{\text{FE}}^{T(0)} / \mathcal{H}_C^{(0)}| \sim \beta^* N \left( \frac{v_F k_F}{\varepsilon_F} \right) \left( \frac{k_F}{\Lambda_0} \right)^2 \ll 1. \quad (47)$$

We see that, because of the small factor  $v_F k_F / \varepsilon_F \ll 1$ , the Coulomb repulsion significantly exceeds the attraction due to phonons, thus completely suppressing superconductivity in this channel.

On the other hand, the analogous estimate for the vector-type  $p$ -wave pairing channel  $F_2^i$ , which, according to Table II, is also attractive if only the transverse phonons are considered, gives

$$|\mathcal{H}_{\text{FE}}^{T(2)} / \mathcal{H}_C^{(2)}| \sim \alpha^* \beta^* N^2 \left( \frac{k_F(l_r)}{\Lambda_0} \right)^2, \quad (48)$$

where we explicitly restore the argument  $l_r$ . We see that, unlike the  $s$ -wave, the above expression does not have the smallness  $v_F k_F / \varepsilon_F$ . Consequently, assuming that  $\alpha^*, \beta^* \sim 1$ , the ratio (48) can be of the order of 1 provided the smallness  $k_F(l_r) / \Lambda_0 = k_F / \Lambda_r \sim k_F c_{T0} / \omega_{T0}$  is compensated by a large numerical prefactor and a large number of Dirac cones  $N$ .

The prerequisites for the  $p$ -wave superconductivity in the scenario described above impose a lot of constraints on the parameters entering the problem. It is important to note that the spin-orbit effects are suppressed in the limit  $v_F k_F \ll \varepsilon_F = \sqrt{m^2 + v_F^2 k_F^2}$  (the dispersion becomes effectively Schrödinger-like), which results in the small prefactor  $v_F^2 k_F^2 / \varepsilon_F^2$  in the effective interactions (30) and (38). Because of this additional density dependence in the exponent that dictates  $T_c$ , the TO phonon-mediated mechanism is not parameterically greater than the standard acoustic phonon mechanism. Thus, the two mechanisms must be numerically compared to dictate which one gives a

larger  $T_c$ . Nonetheless, for low-density systems, where the density of states is small, they are both expected to give very small transition temperatures.

## VI. CONCLUSIONS

We have studied the ferroelectric quantum critical point in three-dimensional low-density Dirac materials. We derived a general low-energy effective field theory that includes the interaction between soft phonon modes and electrons, as well as Coulomb repulsion. We showed that the dominant interaction between electrons is mediated by the transverse phonon mode, while the Coulomb repulsion is screened by the lattice. Using RG analysis, we demonstrated that the effective low-energy theory flows to a regime with strong electron-phonon coupling. For comparison, we performed a similar analysis for covalent crystals, where the ‘‘ferroelectric’’ transition implies the breaking of inversion symmetry of the lattice without generating an electrical polarization. While the main results in this case are qualitatively the same, the screening of the Coulomb repulsion is much weaker in covalent crystals because of the lack of lattice polarization. We further demonstrated that the proximity to the FE critical point significantly enhances superconductivity. Finally, we showed how the interplay between phonon-mediated attraction and Coulomb repulsion in covalent crystals can, in principle, lead to  $p$ -wave superconductivity.

It is interesting that the problem of a Dirac semimetal undergoing a ferroelectric transition generically flows to strong coupling even in the absence of a finite Fermi surface. This problem can be addressed using the determinantal quantum Monte Carlo method, since it does not suffer from a sign problem. It will be informative to study the fate of the system in the strong-coupling limit, for example, whether the superconducting transition survives, or it is destroyed by strong critical fluctuations.

We also expect that the strong-coupling regime close to the critical point will have experimental consequences. For example, high-accuracy measurements of the phonon dispersion may reveal a  $2k_F$  Kohn anomaly. Furthermore, strong coupling will significantly enhance electron scattering, leading to a strong temperature-dependent resistivity.

Considering our results in a broader context, we expect this mechanism to be relevant to all low-density superconductors that possess a near crossing of conduction and valence bands. As explained in the introduction, this feature applies to almost all low-density superconductors, including bismuth, YPtBi, PbTe, SnTe,  $\text{Sr}_x\text{Bi}_2\text{Se}_3$ , Ge, and  $\text{Sr}_{3-x}\text{SnO}$ . Of particular interest is the quadratic-band-touching semimetal YPtBi, where a similar RG analysis can lead to nontrivial fixed points. Finally, we suggest that the mechanism considered in this work may be relevant to the high- $T_c$  low-density superconductor FeSe, which also possesses a Dirac-like dispersion close to the  $M$  points in the Brillouin zone.

## ACKNOWLEDGMENTS

We thank Patrick Lee, Liang Fu, Hiroki Isobe, Meng Cheng, and Kamran Behnia for illuminating discussions. V.K. is supported by Department of Energy Office of Basic Energy Sciences, Division of Materials Sciences and Engineering under Grant No. DE-SC0018945. Z.B. acknowledges support from the Pappalardo fellowship at MIT.

## APPENDIX A: ONE-LOOP DIAGRAMS

Here, we list the one-loop diagrams that contribute to our renormalization group equations. We start from the action for the covalent crystals by including both the transverse and longitudinal optical phonon modes. The result for the polar case can be deduced by restricting to the diagrams with only transverse phonons (formally, just take the  $e \rightarrow 0, c_L \rightarrow \infty$  limit):

$$\begin{aligned} \mathcal{S} = \int d^4x \left\{ \sum_{n=1}^N \bar{\psi}_n [Z_\psi \gamma_0 \partial_0 + v_F \gamma_j \partial_j] \psi_n + \frac{1}{2} u_j [(-Z_u^2 \partial_0^2 + \omega_T^2) \delta_{jl} - c_T^2 (\nabla^2 \delta_{jl} - \partial_j \partial_l) - c_L^2 \partial_j \partial_l] u_l \right. \\ \left. + V(u_j u_j)^2 + \frac{\epsilon_\infty}{8\pi} (\partial_j \phi)^2 + ie \sum_{n=1}^N \bar{\psi}_n \gamma^0 \psi_n \phi + \lambda \sum_{n=1}^N \bar{\psi}_n \gamma_0 \gamma_j \psi_n u_j \right\}. \end{aligned} \quad (\text{A1})$$

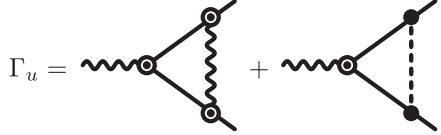
In this paper, we use the standard momentum-shell RG scheme, implying integrating out an infinitesimal momentum shell  $\Lambda_0 e^{-\delta l} < q < \Lambda_0$  and all frequencies  $-\infty < \omega < \infty$  at every RG step.

### 1. Fermion self-energy

Both the optical phonons and the Coulomb field contribute to the fermion self-energy. The contributions from the phonon fields come from both the transverse phonon field and the longitudinal phonon field:



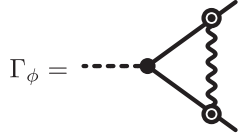




$$\begin{aligned}
 \Gamma_u &= \text{Diagram 1} + \text{Diagram 2} \\
 &= -\lambda \frac{(-\lambda)^2}{(2\pi)^4} \int d^4p \frac{\delta_{jn} - \hat{p}_j \hat{p}_n}{(Z_u p_0)^2 + (c_T \mathbf{p})^2} \gamma_0 \gamma_j \frac{-i}{Z_\psi p_0 \gamma_0 + v_F \mathbf{p} \cdot \boldsymbol{\gamma}} \gamma_0 \gamma_l \frac{-i}{Z_\psi p_0 \gamma_0 + v_F \mathbf{p} \cdot \boldsymbol{\gamma}} \gamma_0 \gamma_n \\
 &\quad - \lambda \frac{(-\lambda)^2}{(2\pi)^4} \int d^4p \frac{\hat{p}_j \hat{p}_n}{(Z_u p_0)^2 + (c_L \mathbf{p})^2} \gamma_0 \gamma_j \frac{-i}{Z_\psi p_0 \gamma_0 + v_F \mathbf{p} \cdot \boldsymbol{\gamma}} \gamma_0 \gamma_l \frac{-i}{Z_\psi p_0 \gamma_0 + v_F \mathbf{p} \cdot \boldsymbol{\gamma}} \gamma_0 \gamma_n \\
 &\quad - \lambda \frac{(-ie)^2}{(2\pi)^4} \int d^4p \frac{4\pi}{\varepsilon_\infty \mathbf{p}^2} \gamma_0 \frac{-i}{Z_\psi p_0 \gamma_0 + v_F \mathbf{p} \cdot \boldsymbol{\gamma}} \gamma_0 \gamma_l \frac{-i}{Z_\psi p_0 \gamma_0 + v_F \mathbf{p} \cdot \boldsymbol{\gamma}} \gamma_0 \\
 &= -\lambda \gamma_0 \gamma_l \left[ \frac{\lambda^2}{6\pi^2 c_T v_F (v_F Z_u + c_T Z_\psi)} - \frac{\lambda^2 \left(1 + \frac{2v_F Z_u}{v_F Z_u + c_L Z_\psi}\right)}{12\pi^2 c_L v_F (v_F Z_u + c_L Z_\psi)} + \frac{e^2}{3\pi v_F Z_\psi \varepsilon_\infty} \right] dl.
 \end{aligned} \tag{A7}$$

### 5. Coulomb vertex correction

The correction to the Coulomb vertex equals

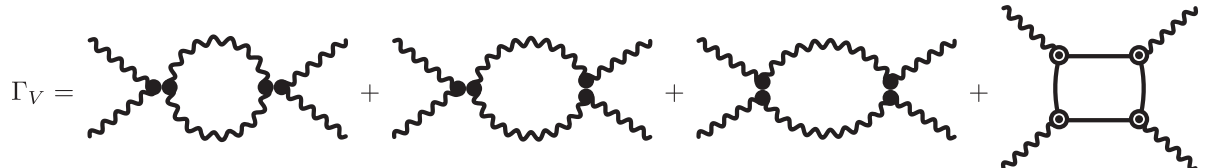


$$\begin{aligned}
 \Gamma_\phi &= \text{Diagram} \\
 &= -ie \frac{(-\lambda)^2}{(2\pi)^4} \int d^4p \frac{\delta_{jn} - \hat{p}_j \hat{p}_n}{(Z_u p_0)^2 + (c_T \mathbf{p})^2} \gamma_0 \gamma_j \frac{-i}{Z_\psi p_0 \gamma_0 + v_F \mathbf{p} \cdot \boldsymbol{\gamma}} \gamma_0 \frac{-i}{Z_\psi p_0 \gamma_0 + v_F \mathbf{p} \cdot \boldsymbol{\gamma}} \gamma_0 \gamma_n \\
 &\quad - ie \frac{(-\lambda)^2}{(2\pi)^4} \int d^4p \frac{\hat{p}_j \hat{p}_n}{(Z_u p_0)^2 + (c_L \mathbf{p})^2} \gamma_0 \gamma_j \frac{-i}{Z_\psi p_0 \gamma_0 + v_F \mathbf{p} \cdot \boldsymbol{\gamma}} \gamma_0 \frac{-i}{Z_\psi p_0 \gamma_0 + v_F \mathbf{p} \cdot \boldsymbol{\gamma}} \gamma_0 \gamma_n \\
 &= -ie \gamma_0 \left[ \frac{\lambda^2 Z_u}{2\pi^2 c_T (v_F Z_u + c_T Z_\psi)^2} + \frac{\lambda^2 Z_u}{4\pi^2 c_L (v_F Z_u + c_L Z_\psi)^2} \right] dl.
 \end{aligned} \tag{A8}$$

Note that the one-loop  $\sim e^3$  vertex correction vanishes in the case of the instantaneous Coulomb interaction.

### 6. Phonon interaction vertex correction

Finally, the four-phonon vertex is renormalized by the phonon bubble diagrams and by the fermion box diagram. Overall, we find that the correction is given by



$$\begin{aligned}
 \Gamma_V &= \text{Diagram 1} + \text{Diagram 2} + \text{Diagram 3} + \text{Diagram 4} \\
 &= \left( \frac{17V^2}{5\pi^2 Z_u c_T^3} + \frac{47V^2}{30\pi^2 Z_u c_L^3} + \frac{16V^2}{15\pi^2 Z_u c_T c_L (c_T + c_L)} + \frac{\lambda^4 N}{24\pi^2 Z_\psi v_F^3} \right) dl.
 \end{aligned} \tag{A9}$$

## APPENDIX B: RG EQUATIONS FOR IONIC CRYSTALS ( $Q \neq 0$ )

As explained in Sec. IV A, in the ionic case the, dipolar interactions between lattice distortions generate a big mass  $\omega_L$  for longitudinal phonons, which effectively screen the Coulomb repulsion between electrons. As a result, the Coulomb interaction and longitudinal phonons become irrelevant for our renormalization group study. Thus, the RG equations for the ionic case can be easily derived from the calculations in Appendix A by setting  $e = 0$  and  $c_L \rightarrow \infty$ . This limit leads to the following RG equations:

$$\frac{dZ_\psi}{dl} = \left[ 2\eta_\psi - 2z - 3 + \frac{\lambda^2 Z_u}{2\pi^2 c_T (c_T Z_\psi + v_F Z_u)^2} \right] Z_\psi, \quad (\text{B1})$$

$$\frac{dv_F}{dl} = \left[ 2\eta_\psi - z - 4 + \frac{\lambda^2 Z_u}{6\pi^2 c_T (c_T Z_\psi + v_F Z_u)^2} \right] v_F, \quad (\text{B2})$$

$$\frac{dZ_u^2}{dl} = (2\eta_u - 3z - 3)Z_u^2 + \frac{N\lambda^2 Z_\psi}{12\pi^2 v_F^3}, \quad (\text{B3})$$

$$\frac{dc_T^2}{dl} = (2\eta_u - z - 5)c_T^2 - \frac{N\lambda^2}{12\pi^2 Z_\psi v_F}, \quad (\text{B4})$$

$$\frac{d\omega_T^2}{dl} = (2\eta_u - z - 3)\omega_T^2 - \frac{N\lambda^2 \Lambda_0^2}{3\pi^2 Z_\psi v_F} + \frac{10\Lambda_0^2 V}{3\pi^2 c_T Z_u}, \quad (\text{B5})$$

$$\frac{d\lambda}{dl} = (2\eta_\psi + \eta_u - 2z - 6)\lambda + \frac{\lambda^3}{6\pi^2 c_T v_F (v_F Z_u + c_T Z_\psi)}, \quad (\text{B6})$$

$$\frac{dV}{dl} = (4\eta_u - 3z - 9)V - \frac{17V^2}{5\pi^2 c_T^3 Z_u} - \frac{\lambda^4 N}{24\pi^2 Z_\psi v_F^3}. \quad (\text{B7})$$

## APPENDIX C: RG EQUATIONS FOR COVALENT CRYSTALS ( $Q=0$ )

The RG equations for the covalent case can be readily obtained from Eqs. (A2)–(A9):

$$\frac{dZ_\psi}{dl} = \left[ 2\eta_\psi - 2z - 3 + \frac{\lambda^2 Z_u}{2\pi^2 c_T (c_T Z_\psi + v_F Z_u)^2} + \frac{\lambda^2 Z_u}{4\pi^2 c_L (c_L Z_\psi + v_F Z_u)^2} \right] Z_\psi, \quad (\text{C1})$$

$$\frac{dv_F}{dl} = \left[ 2\eta_\psi - z - 4 + \frac{\lambda^2 Z_u}{6\pi^2 c_T (c_T Z_\psi + v_F Z_u)^2} - \frac{\lambda^2 Z_u (3v_F Z_u + 2c_L Z_\psi)}{12\pi^2 c_L v_F Z_u (c_L Z_\psi + v_F Z_u)^2} + \frac{2e^2}{3\pi \epsilon_\infty Z_\psi v_F} \right] v_F, \quad (\text{C2})$$

$$\frac{dZ_u^2}{dl} = (2\eta_u - 3z - 3)Z_u^2 + \frac{N\lambda^2 Z_\psi}{12\pi^2 v_F^3}, \quad (\text{C3})$$

$$\frac{dc_T^2}{dl} = (2\eta_u - z - 5)c_T^2 - \frac{N\lambda^2}{12\pi^2 Z_\psi v_F}, \quad (\text{C4})$$

$$\frac{dc_L^2}{dl} = (2\eta_u - z - 5)c_L^2 + \frac{N\lambda^2}{12\pi^2 Z_\psi v_F}, \quad (\text{C5})$$

$$\frac{d\omega_T^2}{dl} = (2\eta_u - z - 3)\omega_T^2 - \frac{N\lambda^2 \Lambda_0^2}{3\pi^2 Z_\psi v_F} + \frac{5\Lambda_0^2 V}{3\pi^2 Z_u} \left( \frac{2}{c_T} + \frac{1}{c_L} \right), \quad (\text{C6})$$

$$\frac{d\epsilon_\infty}{dl} = (2\eta_\phi - z - 5)\epsilon_\infty + \frac{2Ne^2}{3\pi Z_\psi v_F}, \quad (\text{C7})$$

$$\frac{d\lambda}{dl} = (2\eta_\psi + \eta_u - 2z - 6)\lambda + \frac{\lambda^3}{6\pi^2 c_T v_F (v_F Z_u + c_T Z_\psi)} - \frac{\lambda^3 (3v_F Z_u + c_L Z_\psi)}{12\pi^2 c_L v_F (v_F Z_u + c_L Z_\psi)^2} + \frac{\lambda e^2}{3\pi v_F Z_\psi \epsilon_\infty}, \quad (\text{C8})$$

$$\frac{de}{dl} = (2\eta_\psi + \eta_\phi - 2z - 6)e + \frac{e\lambda^2 Z_u}{2\pi^2 c_T (v_F Z_u + c_T Z_\psi)^2} + \frac{e\lambda^2 Z_u}{4\pi^2 c_L (v_F Z_u + c_L Z_\psi)^2}, \quad (\text{C9})$$

$$\frac{dV}{dl} = (4\eta_u - 3z - 9)V - \frac{\lambda^4 N}{24\pi^2 Z_\psi v_F^3} - \frac{17V^2}{5\pi^2 Z_u c_T^3} - \frac{47V^2}{30\pi^2 Z_u c_L^3} - \frac{16V^2}{15\pi^2 Z_u c_T c_L (c_T + c_L)}. \quad (\text{C10})$$

It is worth noticing that the one-loop  $\sim e^3$  correction to  $e$  in Eq. (C9) vanishes in the case of the instantaneous Coulomb interaction.

## APPENDIX D: COMMENTS ABOUT CRYSTAL ANISOTROPY

In the analysis presented in the main text, we consider a fully rotational invariant system. In a realistic crystal, however, there are always anisotropies. In this Appendix, we discuss such anisotropies in ionic crystals with cubic symmetry.

A cubic anisotropy has two important effects that are relevant to the flow of  $\beta$ . First, the dispersion of the soft modes (3) includes the anisotropy term

$$S_u^a = -\kappa \int d^4 q q_j^2 u_j^2.$$

We neglect this term in what follows; i.e., we assume  $\kappa = 0$ . We also mention a recent comment where the effect of this

term on the polarization of the ferroelectric modes is computed perturbatively [48].

The second effect of crystal anisotropy which we consider appears in the electronic dispersion, which is relevant only for  $N > 1$ . Let us consider  $N = 4$ , where the four Dirac points occur on the boundary of the BZ at the  $L$  points. In this case, the Dirac dispersion term Eq. (2) is modified according to [61]

$$\begin{aligned} \mathcal{S}_\psi = \sum_{n=1}^N \int d^4x \bar{\psi}_n & [\gamma_0 \partial_0 + v_F (\gamma_x \partial_x + \gamma_y \partial_y) \\ & + v_z \gamma_z \partial_z + m - \gamma_0 \epsilon_F] \psi_n, \end{aligned} \quad (\text{D1})$$

where the  $z$  direction is defined differently for each Dirac point. It corresponds to the line connecting the  $\Gamma$  point to each of the  $L$  points. Additionally, the coupling of each of these Dirac points to the phonons Eq. (7) is also modified:

$$\mathcal{S}_{\psi u} = \sum_{n=1}^N \int d^4x \bar{\psi}_n [\lambda_z \gamma_0 \gamma_z u_z + \lambda (\gamma_0 \gamma_x u_x + \gamma_0 \gamma_y u_y)] \psi_n, \quad (\text{D2})$$

where  $\lambda_z$  is the coupling to a distortion along the line and  $\lambda$  is the coupling transverse to it.

The RG procedure described in Sec. IV can still be performed analytically, although the expressions become rather lengthy. We also have two additional dimensionless parameters  $v_z/v_F$  and  $\lambda_z/\lambda$  that flow under the RG.

The crucial point is that the main result of this paper, the flow of  $\beta$  towards strong coupling, remains unchanged. To demonstrate this point, we plot the  $\beta$  function for  $\beta$  in the anisotropic case normalized by the  $\beta$  function for isotropic case, Eq. (17), with  $\zeta_T = 0.1$  in Fig. 7. Here, the ratio is plotted for three different values of  $\lambda_z/\lambda$  as a function of  $v_z/v_F$ . We find that in all cases the  $\beta$  function is positive. Also note that the regimes of  $v_z < v_F$  and  $v_z > v_F$  should not be considered on equal footing, since in the latter case

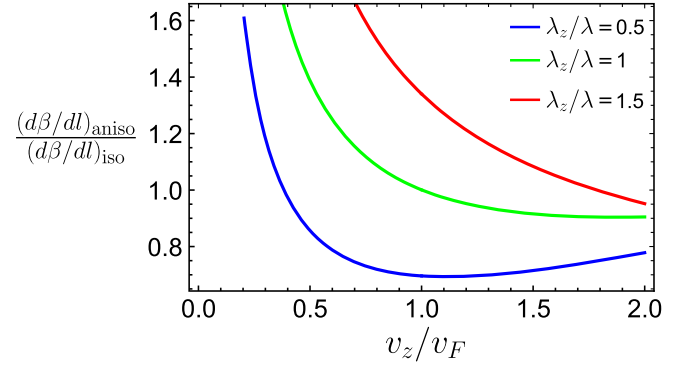


FIG. 7. The  $\beta$ -function for the flow of the dimensionless coupling constant  $\beta$  with the anisotropies, Eqs. (D1)–(D2), normalized by the “isotropic”  $\beta$ -function given by Eq. (17), as a function of  $v_z/v_F$  for three different values of  $\lambda_z/\lambda$ .

the density of states at the Dirac point is enhanced, while in the opposite limit it is decreased. Also, note that we do not perform a detailed study of the multidimensional flow in the four-dimensional space of all four parameters.

## APPENDIX E: DECOMPOSITION OF THE EFFECTIVE INTERACTION INTO PAIRING CHANNELS

In this Appendix, we briefly outline the procedure for the decomposition of the effective interaction into the pairing channels. As an example, we consider the Coulomb interaction given by Eq. (42), while the decomposition of the phonon-mediated interactions (30) and (38) can be performed analogously. Considering only pairings with zero total momentum, we find that Eq. (42) can be written as

$$\mathcal{H}_C \approx \sum_{\mathbf{k}, \mathbf{p}} V_{\alpha\beta\gamma\delta}(\mathbf{k}, \mathbf{p}) c_{\mathbf{p}\alpha}^\dagger c_{-\mathbf{p}\beta}^\dagger c_{-\mathbf{k}\gamma} c_{\mathbf{k}\delta}, \quad (\text{E1})$$

where  $V_{\alpha\beta\gamma\delta}(\mathbf{k}, \mathbf{p})$  is given by

$$\begin{aligned} V_{\alpha\beta\gamma\delta}(\mathbf{k}, \mathbf{p}) = 4\pi\alpha^* v_F & \left\{ \frac{1}{(\mathbf{p} - \mathbf{k})^2 + q_{\text{TF}}^2} [(\beta_+^2 + \beta_-^2(\hat{\mathbf{p}} \cdot \hat{\mathbf{k}})) + i\beta_-^2 \hat{\mathbf{p}} \times \hat{\mathbf{k}} \cdot \boldsymbol{\sigma}]_{\alpha\delta} \times [(\beta_+^2 + \beta_-^2(\hat{\mathbf{p}} \cdot \hat{\mathbf{k}})) + i\beta_-^2 \hat{\mathbf{p}} \times \hat{\mathbf{k}} \cdot \boldsymbol{\sigma}]_{\beta\gamma} \right. \\ & \left. - \frac{1}{(\mathbf{p} + \mathbf{k})^2 + q_{\text{TF}}^2} [(\beta_+^2 - \beta_-^2(\hat{\mathbf{p}} \cdot \hat{\mathbf{k}})) - i\beta_-^2 \hat{\mathbf{p}} \times \hat{\mathbf{k}} \cdot \boldsymbol{\sigma}]_{\alpha\gamma} \times [(\beta_+^2 - \beta_-^2(\hat{\mathbf{p}} \cdot \hat{\mathbf{k}})) - i\beta_-^2 \hat{\mathbf{p}} \times \hat{\mathbf{k}} \cdot \boldsymbol{\sigma}]_{\beta\delta} \right\}, \end{aligned} \quad (\text{E2})$$

and we took into account only states near Fermi surface,  $|\mathbf{k}| \approx |\mathbf{p}| \approx k_F$ . Then, this interaction can be decomposed into the pairing channels according to

$$V_{\alpha\beta\gamma\delta}(\mathbf{k}, \mathbf{p}) = \frac{\pi\alpha^* v_F}{k_F^2} \sum_{n=0}^2 f_n \left( \frac{q_{\text{TF}}}{k_F} \right) \sum_j [iF_n^j(\hat{\mathbf{p}})\sigma_y]_{\alpha\beta} [iF_n^j(\hat{\mathbf{k}})\sigma_y]_{\gamma\delta}^\dagger + \dots, \quad (\text{E3})$$

where form factors  $F_n^j$  are defined in Table II. Next, multiplying this expression by  $[iF_n^j(\hat{\mathbf{k}})\sigma_y]_{\delta\gamma}$ , performing the summation over spin indices  $\gamma$  and  $\delta$  using Fierz identities, and evaluating the integral over  $\hat{\mathbf{k}}$ , we find

$$\begin{aligned}
f_0(x) &= (\beta_+^4 + \beta_-^4) \ln \frac{4+x^2}{x^2} + \beta_+^2 \beta_-^2 \left[ -4 + (2+x^2) \ln \frac{4+x^2}{x^2} \right], \\
f_1(x) &= 2\beta_+^2 \beta_-^2 \ln \frac{4+x^2}{x^2} + \frac{\beta_+^4 + \beta_-^4}{2} \left[ -4 + (2+x^2) \ln \frac{4+x^2}{x^2} \right], \\
f_2(x) &= \frac{3\beta_+^2 \beta_-^2}{4} \left[ -2(2+x^2) + \frac{4+(2+x^2)^2}{2} \ln \frac{4+x^2}{x^2} \right] + \frac{3(\beta_+^4 + \beta_-^4)}{2} \left[ -2 + \frac{2+x^2}{2} \ln \frac{4+x^2}{x^2} \right]. \quad (\text{E4})
\end{aligned}$$

The asymptotic behavior of these expressions in the limit  $k_F v_F \ll \varepsilon_F = \sqrt{m^2 + k_F^2 v_F^2}$  (which corresponds to  $x \gg 1$ ) is presented in the main text; see Eq. (46).

- 
- [1] V. V. Tolmachev and S. V. Tiablikov, *A New Method in the Theory of Superconductivity II*, Sov. Phys. JETP **7**, 46 (1958).
- [2] N. N. Bogoliubov, V. V. Tolmachev, and D. V. Shirkov, *A New Method in the Theory of Superconductivity* (Consultants Bureau, New York, 1958), translation.
- [3] P. Morel and P. W. Anderson, *Calculation of the Superconducting State Parameters with Retarded Electron-Phonon Interaction*, Phys. Rev. **125**, 1263 (1962).
- [4] J. F. Schooley, W. R. Hosler, and M. L. Cohen, *Superconductivity in Semiconducting SrTiO<sub>3</sub>*, Phys. Rev. Lett. **12**, 474 (1964).
- [5] E. Bustarret, *Superconducting Diamond: An Introduction*, Phys. Status Solidi (a) **205**, 997 (2008).
- [6] Superconductivity has been measured in Zr-doped SrTiO<sub>3</sub>, where the density is argued to be even lower [7].
- [7] D. M. Eagles, *Comment on Two Papers Claiming Records for the Lowest Carrier Concentration at Which Superconductivity Has Been Observed*, arXiv:1604.05660.
- [8] Y. Matsushita, P. A. Wiannecki, A. T. Sommer, T. H. Geballe, and I. R. Fisher, *Type II Superconducting Parameters of Tl-Doped PbTe Determined from Heat Capacity and Electronic Transport Measurements*, Phys. Rev. B **74**, 134512 (2006).
- [9] Z. Liu, X. Yao, J. Shao, M. Zuo, L. Pi, S. Tan, C. Zhang, and Y. Zhang, *Superconductivity with Topological Surface State in Sr<sub>x</sub>Bi<sub>2</sub>Se<sub>3</sub>*, J. Am. Chem. Soc. **137**, 10512 (2015).
- [10] N. P. Butch, P. Syers, K. Kirshenbaum, A. P. Hope, and J. Paglione, *Superconductivity in the Topological Semimetal YPtBi*, Phys. Rev. B **84**, 220504(R) (2011).
- [11] X. Lin, G. Bridoux, A. Gourgout, G. Seyfarth, S. Krämer, M. Nardone, B. Fauqué, and K. Behnia, *Critical Doping for the Onset of a Two-Band Superconducting Ground State in SrTiO<sub>3-δ</sub>*, Phys. Rev. Lett. **112**, 207002 (2014).
- [12] T. M. Bretz-Sullivan, A. Edelman, J. S. Jiang, A. Suslov, D. Graf, J. Zhang, G. Wang, C. Chang, J. E. Pearson, A. B. Martinson *et al.*, *Superconductivity in the Dilute Single Band Limit in Reduced Strontium Titanate*, arXiv:1904.03121.
- [13] O. Prakash, A. Kumar, A. Thamizhavel, and S. Ramakrishnan, *Evidence for Bulk Superconductivity in Pure Bismuth Single Crystals at Ambient Pressure*, Science **355**, 52 (2017).
- [14] V. L. Gurevich, A. I. Larkin, and Yu. A. Firsov, *On the Possibility of Superconductivity in Semiconductors*, Sov. Phys. Solid State **4**, 131 (1962).
- [15] Y. Takada, *Theory of Superconductivity in Polar Semiconductors and Its Application to N-Type Semiconducting SrTiO<sub>3</sub>*, J. Phys. Soc. Jpn. **49**, 1267 (1980).
- [16] L. Savary, J. Ruhman, J. W. F. Venderbos, L. Fu, and P. A. Lee, *Superconductivity in Three-Dimensional Spin-Orbit Coupled Semimetals*, Phys. Rev. B **96**, 214514 (2017).
- [17] S. E. Rowley, C. Enderlein, J. F. de Oliveira, D. A. Tompsett, E. B. Saitovitch, S. S. Saxena, and G. G. Lonzarich, *Superconductivity in the Vicinity of a Ferroelectric Quantum Phase Transition*, arXiv:1801.08121.
- [18] M. N. Gastiasoro, A. V. Chubukov, and R. M. Fernandes, *Phonon-Mediated Superconductivity in Low Carrier-Density Systems*, Phys. Rev. B **99**, 094524 (2019).
- [19] Y. Takada, *Plasmon Mechanism of Superconductivity in Two and Three-Dimensional Electron Systems*, J. Phys. Soc. Jpn. **45**, 786 (1978).
- [20] J. Ruhman and P. A. Lee, *Superconductivity at Very Low Density: The Case of Strontium Titanate*, Phys. Rev. B **94**, 224515 (2016).
- [21] J. Ruhman and P. A. Lee, *Pairing from Dynamically Screened Coulomb Repulsion in Bismuth*, Phys. Rev. B **96**, 235107 (2017).
- [22] C. S. Koonce, M. L. Cohen, J. F. Schooley, W. R. Hosler, and E. R. Pfeiffer, *Superconducting Transition Temperatures of Semiconducting SrTiO<sub>3</sub>*, Phys. Rev. **163**, 380 (1967).
- [23] G. Binnig, A. Baratoff, H. E. Hoening, and J. G. Bednorz, *Two-Band Superconductivity in Nb-Doped SrTiO<sub>3</sub>*, Phys. Rev. Lett. **45**, 1352 (1980).
- [24] J. Appel, *Soft-Mode Superconductivity in SrTiO<sub>3-x</sub>*, Phys. Rev. **180**, 508 (1969).
- [25] Y. Matsushita, H. Bluhm, T. H. Geballe, and I. R. Fisher, *Evidence for Charge Kondo Effect in Superconducting Tl-Doped PbTe*, Phys. Rev. Lett. **94**, 157002 (2005).
- [26] D. M. Eagles, *Possible Pairing without Superconductivity at Low Carrier Concentrations in Bulk and Thin-Film Superconducting Semiconductors*, Phys. Rev. **186**, 456 (1969).
- [27] L. P. Gor'kov, *Back to Mechanisms of Superconductivity in Low-Doped Strontium Titanate*, J. Supercond. Novel Magn. **30**, 845 (2017).
- [28] A. V. Chubukov and J. Schmalian, *Superconductivity due to Massless Boson Exchange in the Strong-Coupling Limit*, Phys. Rev. B **72**, 174520 (2005).
- [29] S. Lederer, Y. Schattner, E. Berg, and S. A. Kivelson, *Enhancement of Superconductivity near a Nematic Quantum Critical Point*, Phys. Rev. Lett. **114**, 097001 (2015).

- [30] M. A. Metlitski, D. F. Mross, S. Sachdev, and T. Senthil, *Cooper Pairing in Non-Fermi Liquids*, *Phys. Rev. B* **91**, 115111 (2015).
- [31] Y. Wang, A. Abanov, B. L. Altshuler, E. A. Yuzbashyan, and A. V. Chubukov, *Superconductivity near a Quantum-Critical Point: The Special Role of the First Matsubara Frequency*, *Phys. Rev. Lett.* **117**, 157001 (2016).
- [32] D. J. Scalapino, *Superconductivity and Spin Fluctuations*, *J. Low Temp. Phys.* **117**, 179 (1999).
- [33] P. J. Hirschfeld, M. M. Korshunov, and I. I. Mazin, *Gap Symmetry and Structure of Fe-Based Superconductors*, *Rep. Prog. Phys.* **74**, 124508 (2011).
- [34] H. Watanabe and A. Vishwanath, *Criterion for Stability of Goldstone Modes and Fermi Liquid Behavior in a Metal with Broken Symmetry*, *Proc. Natl. Acad. Sci. U.S.A.* **111**, 16314 (2014).
- [35] S. E. Rowley, L. J. Spalek, R. P. Smith, M. P. M. Dean, M. Itoh, J. F. Scott, G. G. Lonzarich, and S. S. Saxena, *Ferroelectric Quantum Criticality*, *Nat. Phys.* **10**, 367 (2014).
- [36] W. Jantsch, A. Bussmann-Holder, H. Bilz, and P. Vogl, in *Dynamical Properties of IV-VI Compounds*, edited by G. Holer (Springer, Berlin, 2001), pp. 2001–2002.
- [37] J. M. Edge, Y. Kedem, U. Aschauer, N. A. Spaldin, and A. V. Balatsky, *Quantum Critical Origin of the Superconducting Dome in SrTiO<sub>3</sub>*, *Phys. Rev. Lett.* **115**, 247002 (2015).
- [38] A. Stucky, G. Scheerer, Z. Ren, D. Jaccard, J. M. Poumirol, C. Barreteau, E. Giannini, and D. van der Marel, *Isotope Effect in Superconducting N-Doped SrTiO<sub>3</sub>*, *Sci. Rep.* **6**, 37582 (2016).
- [39] C. W. Rischau, X. Lin, C. P. Grams, D. Finck, S. Harms, J. Engelmayer, T. Lorenz, Y. Gallais, B. Fauqué, J. Hemberger, and K. Behnia, *A Ferroelectric Quantum Phase Transition inside the Superconducting Dome of Sr<sub>1-x</sub>Ca<sub>x</sub>TiO<sub>3δ</sub>*, *Nat. Phys.* **13**, 643 (2017).
- [40] Y. Tomioka, N. Shirakawa, K. Shibuya, and I. H. Inoue, *Enhanced Superconductivity Close to a Non-magnetic Quantum Critical Point in Electron-Doped Strontium Titanate*, *Nat. Commun.* **10**, 738 (2019).
- [41] P. Wölfle and A. V. Balatsky, *Superconductivity at Low Density near a Ferroelectric Quantum Critical Point: Doped SrTiO<sub>3</sub>*, *Phys. Rev. B* **98**, 104505 (2018).
- [42] Y. Kedem, *Novel Pairing Mechanism for Superconductivity at a Vanishing Level of Doping Driven by Critical Ferroelectric Modes*, *Phys. Rev. B* **98**, 220505(R) (2018).
- [43] S. Kanasugi and Y. Yanase, *Spin-Orbit-Coupled Ferroelectric Superconductivity*, *Phys. Rev. B* **98**, 024521 (2018).
- [44] J. R. Arce-Gamboa and G. G. Guzmán-Verri, *Quantum Ferroelectric Instabilities in Superconducting SrTiO<sub>3</sub>*, *Phys. Rev. Mater.* **2**, 104804 (2018).
- [45] G. D. Mahan, in *Polarons in Ionic Crystals and Polar Semiconductors*, edited by J. T. Devreese (North-Holland, Amsterdam, 1972).
- [46] N. W. Ashcroft and N. D. Mermin, *Solid State Physics* (Holt, Rinehart and Winston, New York, 1976).
- [47] G. D. Mahan, *Many-Particle Physics* (Springer Science, New York, 2013).
- [48] J. Ruhman and P. A. Lee, *Comment on “Superconductivity at Low Density near a Ferroelectric Quantum Critical Point: Doped SrTiO<sub>3</sub>”*, [arXiv:1901.11065](https://arxiv.org/abs/1901.11065).
- [49] D. van der Marel, F. Barantani, and C. W. Rischau, *A Possible Mechanism for Superconductivity in Doped SrTiO<sub>3</sub>*, [arXiv:1903.08394](https://arxiv.org/abs/1903.08394).
- [50] D. E. Khmel'nitskii and V. L. Shneerson, *Low-Temperature Displacement-Type Phase Transition in Crystals*, *Sov. Phys. Solid State* **13**, 687 (1971).
- [51] B. A. Strukov and A. P. Levanyuk, *Ferroelectric Phenomena in Crystals: Physical Foundations* (Springer Science, New York, 2012).
- [52] O. E. Kvyatkovskii, *Quantum Effects in Incipient and Low-Temperature Ferroelectrics (A Review)*, *Phys. Solid State* **43**, 1401 (2001).
- [53] R. Roussev and A. J. Millis, *Quantum Critical Effects on Transition Temperature of Magnetically Mediated p-Wave Superconductivity*, *Phys. Rev. B* **63**, 140504(R) (2001).
- [54] H. Fröhlich, H. Pelzer, and S. Zienau, *XX. Properties of Slow Electrons in Polar Materials*, *Philos. Mag. (1798-1977)* **41**, 221 (1950).
- [55] G. D. Mahan, *Temperature Dependence of the Band Gap in CdTe*, *J. Phys. Chem. Solids* **26**, 751 (1965).
- [56] B. Ya. Shapiro, *The Transverse Optical Mode and High Temperature Superconductivity*, *Phys. Lett. A* **127**, 239 (1988).
- [57] L. Fu, *Parity-Breaking Phases of Spin-Orbit-Coupled Metals with Gyrotropic, Ferroelectric, and Multipolar Orders*, *Phys. Rev. Lett.* **115**, 026401 (2015).
- [58] V. Kozii and L. Fu, *Odd-Parity Superconductivity in the Vicinity of Inversion Symmetry Breaking in Spin-Orbit-Coupled Systems*, *Phys. Rev. Lett.* **115**, 207002 (2015).
- [59] P. Hosur, S. A. Parameswaran, and A. Vishwanath, *Charge Transport in Weyl Semimetals*, *Phys. Rev. Lett.* **108**, 046602 (2012).
- [60] H. Isobe and N. Nagaosa, *Theory of a Quantum Critical Phenomenon in a Topological Insulator: (3 + 1)-Dimensional Quantum Electrodynamics in Solids*, *Phys. Rev. B* **86**, 165127 (2012).
- [61] T. H. Hsieh, H. Lin, J. Liu, W. Duan, A. Bansil, and L. Fu, *Topological Crystalline Insulators in the SnTe Material Class*, *Nat. Commun.* **3**, 982 (2012).
- [62] T. Liang, S. Kushwaha, J. Kim, Q. Gibson, J. Lin, N. Kioussis, R. J. Cava, and N. P. Ong, *A Pressure-Induced Topological Phase with Large Berry Curvature in Pb<sub>1-x</sub>Sn<sub>x</sub>Te*, *Sci. Adv.* **3**, e1602510 (2017).
- [63] R. V. Parfen, D. V. Shamshur, and S. A. Némov, *Superconductivity of (Sn<sub>1-z</sub>Pb<sub>z</sub>)<sub>1-x</sub>In<sub>x</sub>Te Alloys*, *Phys. Solid State* **43**, 1845 (2001).
- [64] P. Giraldo-Gallo, P. Walmsley, B. Sangiorgio, S. C. Riggs, R. D. McDonald, L. Buchauer, B. Fauqué, C. Liu, N. A. Spaldin, A. Kaminski, K. Behnia, and I. R. Fisher, *Evidence of Incoherent Carriers Associated with Resonant Impurity Levels and Their Influence on Superconductivity in the Anomalous Superconductor Pb<sub>1-x</sub>Tl<sub>x</sub>Te*, *Phys. Rev. Lett.* **121**, 207001 (2018).
- [65] Note that here we neglect the fast dynamics of the electromagnetic gauge field, and, as a consequence, the electric field is purely longitudinal (i.e., it derives from a potential).
- [66] R. H. Lyddane, R. G. Sachs, and E. Teller, *On the Polar Vibrations of Alkali Halides*, *Phys. Rev.* **59**, 673 (1941).

- [67] T. Bzdušek, A. Rüegg, and M. Sgrist, *Weyl Semimetal from Spontaneous Inversion Symmetry Breaking in Pyrochlore Oxides*, *Phys. Rev. B* **91**, 165105 (2015).
- [68] M. E. Fisher, *The Renormalization Group in the Theory of Critical Behavior*, *Rev. Mod. Phys.* **46**, 597 (1974).
- [69] L. Radzihovsky, *Fluctuations and Phase Transitions in Larkin-Ovchinnikov Liquid-Crystal States of a Population-Imbalanced Resonant Fermi Gas*, *Phys. Rev. A* **84**, 023611 (2011).
- [70] V. Kozii, J. Ruhman, L. Fu, and L. Radzihovsky, *Ferromagnetic Transition in a One-Dimensional Spin-Orbit-Coupled Metal and Its Mapping to a Critical Point in Smectic Liquid Crystals*, *Phys. Rev. B* **96**, 094419 (2017).
- [71] In the case of finite (but small)  $\beta_0$  and  $\gamma_0$ ,  $r_0$  in Eq. (20) should be replaced with  $r_0 \rightarrow \tilde{r}_0 = r_0 + (5\gamma_0/3\pi^2) - (2N\beta_0/3\pi)$ .
- [72] J. W. F. Venderbos, V. Kozii, and L. Fu, *Odd-Parity Superconductors with Two-Component Order Parameters: Nematic and Chiral, Full Gap, and Majorana Node*, *Phys. Rev. B* **94**, 180504(R) (2016).
- [73] The pairing channels in the odd-parity sector (which always implies  $S = 1$ ) with  $J > 1$  generally have contributions from the terms with  $L = J - S$  and  $L = J + S$  orbital angular momenta. As a result, the decomposition into these channels is interaction dependent.
- [74] V. P. Mineev and K. V. Samokhin, *Introduction to Unconventional Superconductivity* (CRC Press, Boca Raton, 1999).
- [75] L. P. Gor'kov and T. K. Melik-Barkhudarov, *Contribution to the Theory of Superfluidity in an Imperfect Fermi Gas*, *Sov. Phys. JETP* **13**, 1018 (1961).
- [76] M. K. Jacobsen, W. Liu, and B. Li, *Sound Velocities of PbTe to 14 GPa: Evidence for Coupling between Acoustic and Optic Phonons*, *J. Phys. Condens. Matter* **25**, 365402 (2013).
- [77] J. An, A. Subedi, and D. J. Singh, *Ab Initio Phonon Dispersions for PbTe*, *Solid State Commun.* **148**, 417 (2008).
- [78] B. A. Assaf, T. Phuphachong, V. V. Volobuev, A. Inhofer, G. Bauer, G. Springholz, L. A. De Vaulchier, and Y. Guldner, *Massive and Massless Dirac Fermions in Pb<sub>1-x</sub>Sn<sub>x</sub>Te Topological Crystalline Insulator Probed by Magneto-Optical Absorption*, *Sci. Rep.* **6**, 20323 (2016).